Solid State Research

1998:2

Lincoln Laboratory

MASSACHUSETTS INSTITUTE OF TECHNOLOGY

LEXINGTON, MASSACHUSETTS

355512

ADA355512

This technical report has been reviewed and is approved for publication.

FOR THE COMMANDER

Gary Tutungian
Administrative Contracting Officer
Contracted Support Management

MASSACHUSETTS INSTITUTE OF TECHNOLOGY
LINCOLN LABORATORY

SOLID STATE RESEARCH

QUARTERLY TECHNICAL REPORT

1 FEBRUARY – 30 APRIL 1998

ISSUED 28 OCTOBER 1998

LEXINGTON   MASSACHUSETTS

ABSTRACT

This report covers in detail the research work of the Solid State Division at Lincoln Laboratory for the period 1 February through 30 April 1998. The topics covered are Quantum Electronics, Electro-optical Materials and Devices, Submicrometer Technology, High Speed Electronics, Microelectronics, Analog Device Technology, and Advanced Silicon Technology. Funding is provided by several DoD organizations—including the Air Force, Army, BMDO, DARPA, Navy, NSA, and OSD—and also by the DOE, NASA, and NIST.

TABLE OF CONTENTS

TABLE OF CONTENTS (Continued)

-

LIST OF ILLUSTRATIONS

LIST OF ILLUSTRATIONS (Continued)

LIST OF ILLUSTRATIONS (Continued)

LIST OF ILLUSTRATIONS (Continued)

LIST OF TABLES

INTRODUCTION

1. QUANTUM ELECTRONICS

A real-time, point bioaerosol sensor for early warning of threat bioaerosols has been developed, which is based on laser-induced-fluorescence detection of aerosol particles and incorporates two spectral channels for discrimination of threat aerosols from background aerosols. Field tests at Dugway Proving Ground, Utah, in September 1997 showed that the sensor can detect threat bioaerosols at a concentration of 5–10 particles per liter of air and can discriminate threat aerosols from natural background aerosols.

2. ELECTRO-OPTICAL MATERIALS AND DEVICES

Measurements of analog optical links from 0.1 to 20 GHz have been obtained. Their performance with an Nd:YAG laser has been compared to their performance with semiconductor laser and amplifier sources.

Tapered lasers have been fabricated from a GaInAsSb/AlGaAsSb single-quantum-well structure with threshold current densities as low as 50 A/cm^2 at room temperature. These lasers have exhibited diffraction-limited cw output power up to 600 mW.

3. SUBMICROMETER TECHNOLOGY

The effects of laser fluence and pulse count on irradiation-induced compaction of fused silica have been experimentally investigated using a 193-nm excimer laser source. The amount of laser-induced compaction is shown to depend upon both the total dose and dose rate.

4. HIGH SPEED ELECTRONICS

Field-emitter arrays for use in inductive output amplifiers have been characterized: process modifications have enabled the fabrication of single- and few-tip arrays, and noise characteristics of such arrays have been obtained. Two schemes for protection against gate-to-tip arc currents have been analyzed and shown to be able to provide arc protection while maintaining the ability to modulate the beam at rf.

5. MICROELECTRONICS

An inhomogeneity in the response to back-surface illuminated charge-coupled devices has been found to be related to laser anneal conditions and the presence of a B interstitial defect. Modifying the ion implantation and laser anneal conditions has eliminated the problem throughout the wavelength and temperature regime of interest.

6. ANALOG DEVICE TECHNOLOGY

The accuracy of 2.0-GHz-bandwidth 20-ns-long high-temperature superconductive (HTS) chirp filters has been improved by more than an order of magnitude. These accurate HTS chirp filters have been used with a microwave chirp generator to produce compressed pulses with error sidelobes down by more than 30 dB from the mainlobe.

7. ADVANCED SILICON TECHNOLOGY

In the development of an integrated CCD/CMOS silicon-on-insulator (SOI) technology, SOITEC Unibond SOI material has been selected as the best suited for high-performance CCDs based on detailed materials and electrical evaluation. In addition, CCD and CMOS processes have been modified for integrated 3.3-V operation, and simulations have demonstrated that high-performance 3.3-V CCD operation is possible; and a test reticle set has been designed and the fabrication of the first monolithic low-power CCD/CMOS process begun.

REPORTS ON SOLID STATE RESEARCH

1 FEBRUARY THROUGH 30 APRIL 1998

PUBLICATIONS

Linear and Nonlinear Microwave Dynamics of Vortices in $YBa_2Cu_3O_{7-\delta}$ Thin Films	N. Belk[*] D. E. Oates D. A. Feld G. Dresselhaus[*] M. S. Dresselhaus[*]	*Phys. Rev. B* **56**, 11 966 (1997)
III-V Quantum-Well Structures for High-Speed Electronics	E. R. Brown K. A. McIntosh	In *Advances in Research and Development: Heterojunctions for High-Speed and Infrared Applications*, Vol. 23 of *Thin Films* (Academic, San Diego, 1997), p. 173
Large-Area Back-Illuminated CCD Imager Development	B. E. Burke J. A. Gregory R. W. Mountain B. B. Kosicki E. D. Savoye P. J. Daniels V. S. Dolat T. L. Lind A. H. Loomis D. J. Young G. A. Tonry	*Exp. Astron.* **8**, 31 (1998)
High-Performance GaInAsSb Thermophotovoltaic Devices with an AlGaAsSb Window	H. K. Choi C. A. Wang G. W. Turner M. J. Manfra D. L. Spears G. W. Charache[*] L. R. Danielson[*] D. M. Depoy[*]	*Appl. Phys. Lett.* **71**, 3758 (1997)

[*]Author not at Lincoln Laboratory.

[*]Author not at Lincoln Laboratory.

Chemically Assisted Ion Beam Etching of Submicron Features in GaSb	G. Nagy[*] R. U. Ahmad[*] M. Levy[*] R. M. Osgood, Jr.[*] M. J. Manfra G. W. Turner	*Appl. Phys. Lett.* **72**, 1350 (1998)
Pattern Transfer for Diffractive and Refractive Microoptics	M. B. Stern	*Microelectron. Eng.* **34**, 299 (1997)
Ultralow-Threshold (50 A/cm^2) Strained Single-Quantum-Well GaInAsSb/AlGaAsSb Lasers Emitting at 2.05 μm	G. W. Turner H. K. Choi M. J. Manfra	*Appl. Phys. Lett.* **72**, 876 (1998)

ACCEPTED FOR PUBLICATION

A 1.3-GHz SOI CMOS Test Chip of Low-Power High-Speed Pulse Processing	R. Berger W. G. Lyons A. M. Soares	*J. Solid-State Circuits*
1.5-μm Tapered-Gain-Region Lasers with High CW Output Powers	J. P. Donnelly J. N. Walpole S. H. Groves R. J. Bailey L. J. Missaggia A. Napoleone	*IEEE Photon. Technol. Lett.*
Low Loss High Efficiency and High Power Diode-Pumped Mid-Infrared GaInSb/InAs Quantum Well Lasers	H. Q. Le C. H. Lin[*] S. S. Pei[*]	*Appl. Phys. Lett*
Phase Noise of a Resonant-Tunneling Relaxation Oscillator	S. Verghese C. D. Parker E. R. Brown	*Appl. Phys. Lett.*

---

[*]Author not at Lincoln Laboratory.

Overview of VCSEL Applications   R. C. Williamson   In *Vertical Cavity Surface Emitting Laser,* C. Wilmsen, H. Temkin, and L. Coldren, eds. (Cambridge University Press, Cambridge, England)

PRESENTATIONS[†]

Title	Authors	Venue
Durability of Pellicles for 193-nm Lithography	A. Grenville V. Liberman R. R. Kunz M. Rothschild J. H. C. Sedlacek R. Uttaro C. VanPeski	23rd SPIE International Symposium on Microlithography, Santa Clara, California, 22-27 February 1998
193-nm Lithography: Fundamentals and Issues	R. R. Kunz	
Durability Testing of Optical Coatings for 193-nm Lithographic Applications	V. Liberman M. Rothschild J. H. C. Sedlacek R. Uttaro A. Grenville K. Bates	
Metrology Methods for the Quantification of Edge Roughness	C. M. Nelson S. C. Palmateer T. M. Lyszczarz	

[†]Titles of presentations are listed for information only. No copies are available for distribution.

Line Edge Roughness in Sub-0.18-μm Resist Patterns	S. C. Palmateer S. G. Cann J. E. Curtin S. P. Doran L. M. Eriksen A. R. Forte R. R. Kunz T. M. Lyszczarz C. Nelson M. B. Stern	23rd SPIE International Symposium on Microlithography, Santa Clara, California, 22-27 February 1998
Photolithography at Wavelengths Below 200 nm	M. Rothschild	
Low-Threshold, High-Power, High-Brightness GaInAsSb/AlGaAsSb Quantum-Well Lasers Emitting at 2.05 μm	H. K. Choi G. W. Turner J. N. Walpole Z. L. Liau L. J. Missaggia M. K. Connors M. J. Manfra V. Daneu P. W. O'Brien A. Sanchez-Rubio D. L. Spears	1998 Diode Laser Technology Review, Albuquerque, New Mexico, 2-4 March 1998
1.55-Micron Laser Development	J. N. Walpole J. P. Donnelly S. H. Groves R. J. Bailey L. J. Missaggia A. Napoleone	
Low-Light-Level 640 × 480-Pixel CCD Camera for Night Vision Applications	R. K. Reich B. E. Burke W. H. McGonagle D. M. Craig A. W. Waxman E. D. Savoye B. B. Kosicki	1998 Meeting of the IRIS Specialty Group on Passive Sensors, Albuquerque, New Mexico, 2-4 March 1998

Integrated Optics	L. M. Johnson	Lincoln Laboratory Technical Seminar Series, The University of Michigan Radiation Laboratory, Ann Arbor, Michigan, 12 March 1998
A Very Wideband Compressive Receiver Using High-T_c Superconductive Chirp Filters	W. G. Lyons R. Berger M. M. Seaver R. R. Boisvert P. G. Murphy D. R. Arsenault A. C. Anderson L. M. Johnson T. C. L. G. Sollner L. Oliva[*] W. R. Bang[*] R. Cecchini[*] P. Burke[*] D. Wang[*] A. F. Hinte[*]	1998 Government Microcircuit Applications Conference, Arlington, Virginia, 16-19 March 1998
Resonant-Tunneling Diode Digital Filters	T. C. L. G. Sollner J. P. Sage C-L. Chen P. A. Maki M. A. Hollis R. H. Mathews	
Properties of Grain-Boundary Josephson Junctions at Microwave Frequencies	D. E. Oates Y. M. Habib[*] C. J. Lehner[*] L. R. Vale[*] R. H. Ono[*] G. Dresselhaus[*] M. S. Dresselhaus[*]	Meeting of the American Physical Society, Los Angeles, California, 16-20 March 1998

[*]Author not at Lincoln Laboratory.

Properties of YBCO Grain Boundaries at Microwave Frequencies	D. E. Oates Y. M. Habib[*] C. J. Lehner[*] L. R. Vale[*] R. H. Ono[*] G. Dresselhaus[*] M. S. Dresselhaus[*]	Meeting of the American Physical Society, Los Angeles, California, 16-20 March 1998
Laser Micromachining of Silicon: A New Technique for Fabricating THz Imaging Arrays	C. K. Walker[*] T. M. Bloomstein S. T. Palmacci M. B. Stern J. E. Curtin	SPIE Symposium on Astronomical Telescopes and Instrumentation Quality, Kona, Hawaii, 20-28 March 1998
Photolithography at Wavelengths Below 200 nm	M. Rothschild	Technical Seminar, Taiwan Semiconductor Manufacturing Company, Hsin-Chin, Taiwan, 23 March 1998
Transmission Electron Microscopy Investigation of Titanium Silicide Thin Films	A. F. Myers[*] E. B. Steel[*] L. M. Struck[*] H. I. Liu J. A. Burns	1998 International Conference on Characterization and Metrology for ULSI Technology, Gaithersburg, Maryland, 23-27 March 1998
Topics in 193 nm Lithography	M. Rothschild	First Seminar on 193 nm Optical Lithography in Taiwan, Taipei, Taiwan, 25-27 March 1998
Superconducting Electronics for Signal Processing	T. C. L. G. Sollner K. Berggren D. A. Feld W. G. Lyons D. E. Oates J. P. Sage	Technical Seminar, Princeton University, Princeton, New Jersey, 30 March 1998

---

[*]Author not at Lincoln Laboratory.

Optical Sampling for Analog-to-Digital Converters	J. C. Twichell	Seminar Series on Optics and Quantum Electronics, Massachusetts Institute of Technology, Cambridge, Massachusetts, 1 April 1998
Photomask Materials, Processing, and Related Issues for Projection Lithography at 157 nm	T. M. Bloomstein M. Rothschild S. T. Palmacci M. W. Horn R. B. Goodman D. E. Hardy	Photomask Japan '98, Kanagawa, Japan, 9-10 April 1998
Cooled Yb:YAG for High-Power Solid-State Lasers	T. Y. Fan T. Crow[*] B. Hoden[*] F. Way[*]	International Symposium on Aerospace/Defense Sensing, Simulation and Controls, Orlando, Florida, 13-17 April 1998
Transmission of RF and Microwave Signals over Optical Fibers	R. C. Williamson	Lincoln Laboratory Technical Seminar Series, University of Wisconsin, Racine, Wisconsin, 27 April 1998
B-Cell-Based Sensors for Rapid Bioagent Identification	M. A. Hollis	American Association of Universities Symposium, Washington, D.C., 29 April 1998
MIT Lincoln Laboratory's Microelectronics Laboratory	C. L. Keast	Lincoln Laboratory Technical Seminar Series, Rose-Hulman Institute of Technology, Terre Haute, Indiana, 29 April 1998

---

[*]Author not at Lincoln Laboratory.

ORGANIZATION

SOLID STATE DIVISION

D. C. Shaver, *Head*
R. W. Ralston, *Associate Head*
N. L. DeMeo, Jr., *Assistant*

Z. L. Lemnios, *Senior Staff*

J. W. Caunt, *Assistant Staff*
K. J. Challberg, *Administrative Staff*
J. D. Pendergast, *Administrative Staff*

SUBMICROMETER TECHNOLOGY

M. Rothschild, *Leader*
T. M. Lyszczarz, *Assistant Leader*
T. H. Fedynyshyn, *Senior Staff*
R. R. Kunz, *Senior Staff*

Astolfi, D. K.	Horn, M. W.
Bloomstein, T. M.	Krohn, K. E.
Craig, D. M.	Liberman, V.
DiNatale, W. F.	Maki, P. A.
Doran, S. P.	Palmacci, S. T.
Efremow, N. N., Jr.	Palmateer, S. C.
Forte, A. R.	Sedlacek, J. H. C.
Geis, M. W.	Stern, M. B.
Goodman, R. B.	Uttaro, R. S.

QUANTUM ELECTRONICS

A. Sanchez-Rubio, *Leader*
T. Y. Fan, *Assistant Leader*

Aggarwal, R. L.	Dill, C., III
Buchter, S.	Jeys, T. H.
Cook, C. C.	Le, H. Q.
Daneu, J. L.	Ochoa, J. R.
Daneu, V.	Zayhowski, J. J.
DiCecca, S.	

ELECTRO-OPTICAL MATERIALS AND DEVICES

D. L. Spears, *Leader*
J. C. Twichell, *Assistant Leader*
H. K. Choi, *Senior Staff*
R. C. Williamson, *Senior Staff*

Bailey, R. J.	Liau, Z. L.	O'Donnell, F. J.
Betts, G. E.	Manfra, M. J.	Poillucci, R. J.
Choi, S. S.*	Missaggia, L. J.	Reeder, R. E.
Connors, M. K.	Mull, D. E.	Turner, G. W.
Cronin, S.*	Napoleone, A.	Vineis, C. J.*
Donnelly, J. P.	Nee, P.*	Walpole, J. N.
Goodhue, W. D.	Nitishin, P. M.	Wang, C. A.
Harman, T. C.	Oakley, D. C.	Wasserman, J.

---

*Research Assistant

HIGH SPEED ELECTRONICS

M. A. Hollis, *Leader*
E. R. Brown, *Assistant Leader*[†]

Bozler, C. O.	McIntosh, K. A.
Calawa, A. R.[‡]	Molnar, R. J.
Calawa, S. D.	Parameswaran, L.
Chen, C. L.	Rabe, S.
Graves, C. A.	Rathman, D. D.
Harris, C. T.	Rider, T. H.
Lightfoot, A.	Verghese, S.
Mahoney, L. J.	Young, A. M.
Mathews, R. H.	

ANALOG DEVICE TECHNOLOGY

T. C. L. G. Sollner, *Leader*
L. M. Johnson, *Assistant Leader*
A. C. Anderson, *Senior Staff*

Ala'ilima, T. F.	Macedo, E. M., Jr.
Arsenault, D. R.	Murphy, P. G.
Berggren, K. K.	Oates, D. E.
Boisvert, R. R.	Paul, S. A.
Feld, D. A.	Sage, J. P.
Fitch, G. L.	Santiago, D. D.
Holtham, J. H.	Seaver, M. M.
Lyons, W. G.	Slattery, R. L.

MICROELECTRONICS

B. B. Kosicki, *Leader*
R. K. Reich, *Assistant Leader*
B. E. Burke, *Senior Staff*

Aull, B. F.	Johnson, K. F.
Cooper, M. J.	Lind, T. A.
Daniels, P. J.	Loomis, A. H.
Doherty, C. L., Jr.	McGonagle, W. H.
Dolat, V. S.	O'Mara, D. M.
Donahue, T. C.	Percival, K. A.
Felton, B. J.	Young, D. J.
Gregory, J. A.	

ADVANCED SILICON TECHNOLOGY

C. L. Keast, *Leader*
P. W. Wyatt, *Associate Leader*

Berger, R.	Liu, H. I.
Burns, J. A.	Newcomb, K. L.
Chen, C. K.	Reinold, J. H., Jr.
Davis, P. V.	Sexton, S. V.
D'Onofrio, R. P.	Soares, A. M.
Frankel, R. S.	Suntharalingam, V.
Fritze, M.	Yost, D.-R.
Knecht, J. M.	Young, G. R.

[†]Intergovernmental Personnel Act assignment
[‡]Part Time

1. QUANTUM ELECTRONICS

1.1 BIOAEROSOL FLUORESCENCE SENSOR

A bioaerosol fluorescence sensor has been developed as part of the Army Integrated Biodetection Advanced Technology Demonstration. The sensor, shown in Figure 1-1, is more than an order of magnitude smaller (3.4 cu ft total), lighter (95 lb), and less power consumptive (50 W) than the proof-of-concept sensor developed in 1996 [1],[2]. Moreover, this sensor is self-contained and capable of independently declaring bioagent alarms. The alarm notification is made via both an RS232 and an ethernet data link. Three identical sensors were successfully tested at the 1997 Joint Field Trials (JFT-4), where they each operated for a total of 170 h over a wide range of environmental conditions, including driving rain, snow, and subfreezing temperatures. The sensors demonstrated a threat bioparticle sensitivity of about 5–10 particles per liter of air and also the ability to distinguish threat bioparticles from important interferents, such as diesel exhaust and dust clouds generated by vehicles.

The bioaerosol fluorescence sensor is designed for continuous monitoring of atmospheric bioparticles, and it provides generic detection of threat bioaerosols with an alarm time of less than 1 min. The sensor could be used either to trigger a separate biological-agent identification sensor or, under high threat

316861-1

Figure 1-1. Bioaerosol fluorescence sensor at Lincoln Laboratory. The sensor is completely contained in the silver box mounted on the black tripod. The tube extending 2 ft above the sensor samples air at the same height as the truth sensors (see Figure 1-7). The sensor is shown powered by two battery boxes sitting on the ground.

1

conditions, to provide the actual defensive alarm. In addition, the sensor can give the all clear signal after an attack. The sensor might be deployed individually or as part of a networked array.

Figure 1-2 illustrates the bioparticle sensor concept. Air is drawn through the sensor and illuminated by a uv laser beam. Fluorescence emitted by aerosol particles that pass through the laser beam is incident on two photomultiplier tubes. A uv spectral bandpass (300–400 nm) filter is placed in front of one of the photomultiplier tubes; this tube is sensitive to biofluorescence from the amino acid tryptophan. A visible spectral bandpass (400–600 nm) filter is placed in front of the other photomultiplier tube; this tube is sensitive to biofluorescence from NADH and flavin compounds. The biochemicals tryptophan, NADH, and the flavins are common to all living organisms. The signals from the photodetectors are measured by temporally gated charge integrators and are recorded and analyzed in real time by a microprocessor. Aerosol particles are counted as they pass through the sensor by counting the coincident pulses from the photomultiplier tubes. The normalized difference of the two photomultiplier signals is used to discriminate potential threat bioaerosols from background aerosols.

A more detailed geometry of the sensor optics is shown in Figure 1-3. Air is drawn through a nozzle into the laser interaction region by an exhaust fan. The nozzle exit dimensions are 14 mm wide by 22 mm long. The laser is passed 10 times through the free jet of the nozzle by multiple reflections from two mirrors that are slightly tilted relative to one another, as shown in Figure 1-3(b). Multiple passing of the laser
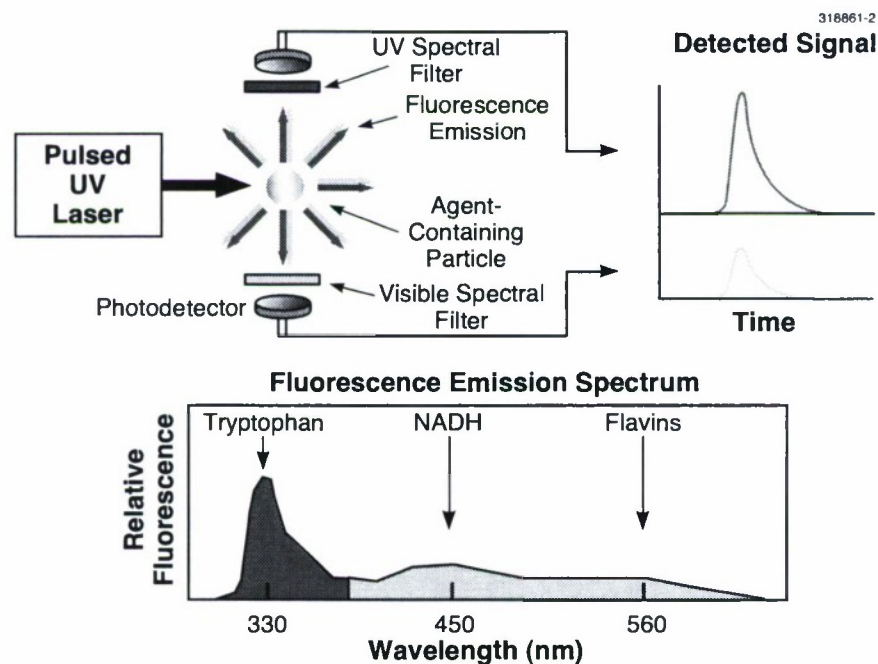
Figure 1-2. Bioaerosol fluorescence sensor concept.
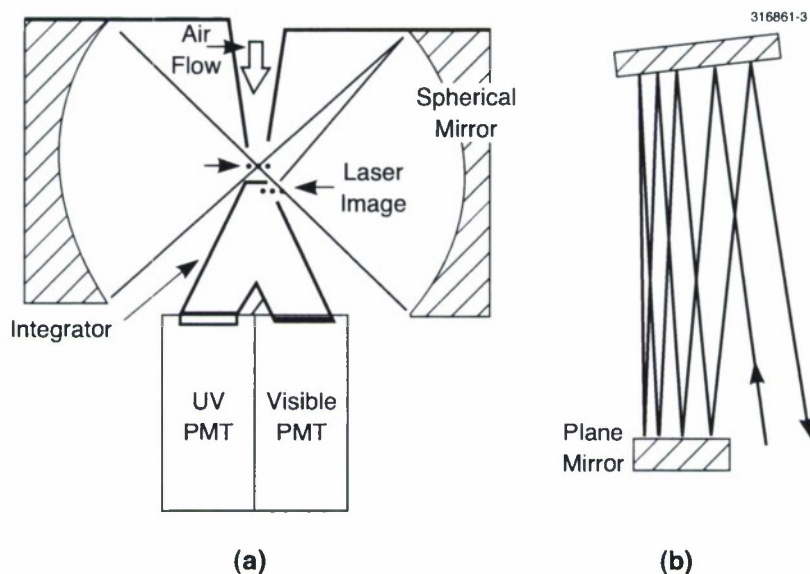
Figure 1-3. Bioaerosol fluorescence sensor detection geometry: (a) signal collection (side view) and (b) multiple passing of laser beam (top view).

beam increases the volume of air that the sensor samples and, thus, increases the sensor sensitivity to low-concentration aerosols. Air flows through the nozzle at a rate of 120 liters per minute; 20 liters per minute are actively sampled by the laser beam. Fluorescence from particles in the air stream is collected by two spherical mirrors (75-mm radius of curvature, 100-mm diameter) and imaged into a light integrator. Imaging of the particle fluorescence provides strong discrimination against stray photons within the interaction chamber. One mirror is placed a distance equal to its radius of curvature from the central laser beam so that this mirror reimages the fluorescence back onto the laser beams and toward the other spherical mirror. The other spherical mirror is placed slightly farther out than its radius of curvature and downward so as to image the collected fluorescence 3 mm to the right and 6 mm below the laser beams and into the 5-mm-tall by 21-mm-long entrance of a light integrator. The fluorescence entering the integrator is internally reflected towards the two photomultipliers. The spherical mirrors and the interior of the integrator are aluminum coated and have normal incidence reflectivities of 80% over the 300–600-nm spectral range. On average the fluorescence radiation makes four mirror reflections prior to passing through the spectral filters and to the photomultipliers.

Each photomultiplier (Hamamatsu R1924) has a 21-mm-diam bialkali photocathode with approximately 20% quantum efficiency. The uv photomultiplier has a 2-mm-thick UG1 Schott glass filter in front of the photocathode; the visible photomultiplier has both 1-mm-thick BG39 and 1-mm-thick CG410 Schott glass filters in front of the photocathode. The spectral transmission of these filters is the same as for

3

those used in the 1996 proof-of-concept sensor [1],[2]. Each photomultiplier signal is measured with a charge-to-digital converter that is temporally gated on for a 40-ns window centered on the laser pulse. The combined photomultiplier temporal response and bioparticle fluorescence lifetime is less than 10 ns. The digitized photomultiplier signals are analyzed by an Intel 486 microprocessor residing inside the sensor housing.

The uv laser beam is produced by a diode-pumped, passively Q-switched Nd:YAG microlaser developed at Lincoln Laboratory [3]. The laser is frequency quadrupled to 266 nm by KTP and BBO crystals. The 266-nm microlaser pulses have an energy of 0.3 μJ, a duration of 400 ps, and a repetition rate of about 10 kHz. The laser beam has a diameter of about 0.5 mm (full width at half-maximum intensity) in the sample air jet.

By using an aerosol chamber in the laboratory, the sensor was exposed to many different kinds of aerosols for the purpose of establishing the aerosol fluorescence spectral signatures. (The threat simulants—*Bacillus subtilis*, *Erwinia herbicola*, MS2 virus—and a sample of the dirt from the JFT-4 test site were provided to us by Dugway Proving Grounds.) The normalized differences of the coincident signals in the uv and visible photomultiplier tubes, on a particle-by-particle basis, for a few bioaerosols are shown in Figure 1-4. As can be seen, the threat simulants have signatures distinguishable from typical natural background aerosols.
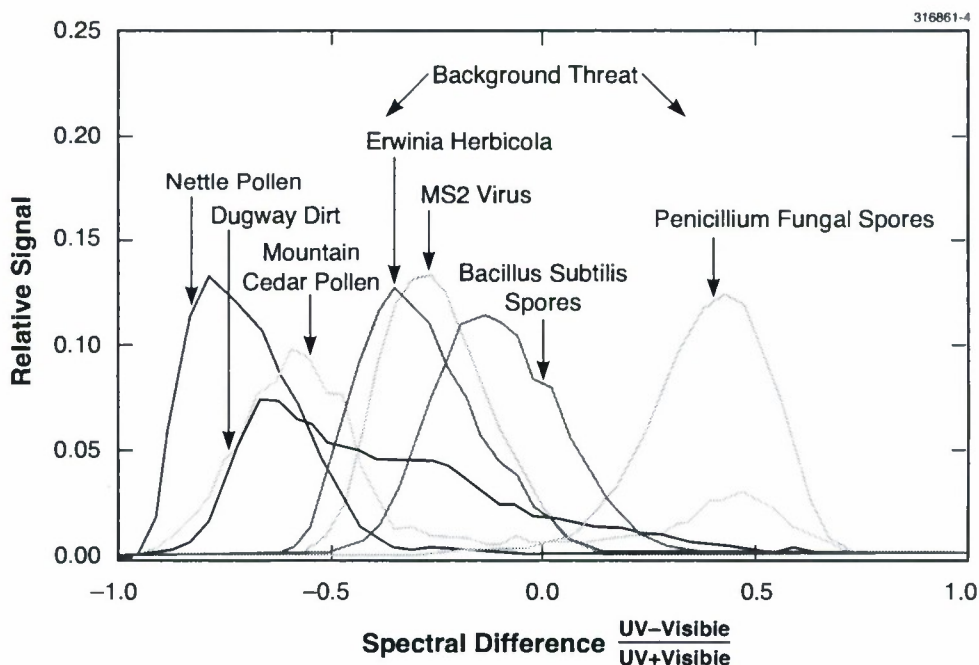
Figure 1-4. Histogram of sensor events as a function of normalized difference of coincident signals in uv and visible photomultipliers for various bioaerosols.

4
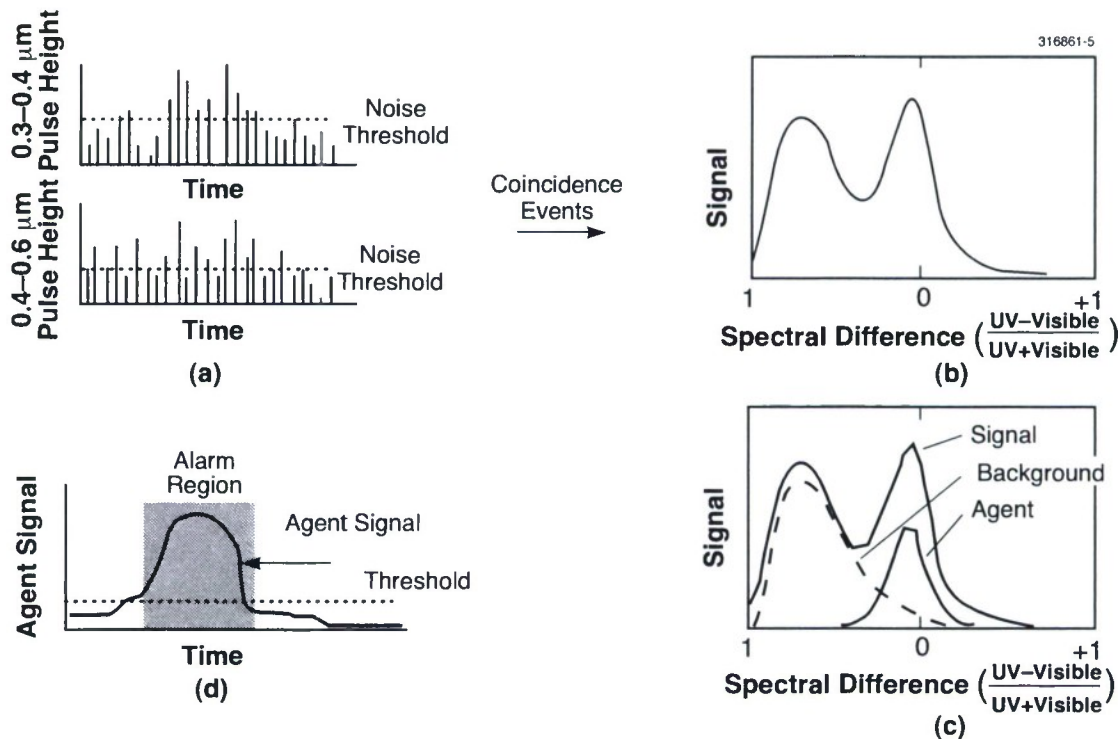
Figure 1-5. Sensor alarm algorithm: (a) pulse-height threshold and coincidence test, (b) spectral histogram, (c) decomposition, and (d) alarm declaration.

The sensor alarm algorithm is illustrated in Figure 1-5. Signals from the uv and visible photomultipliers are first subjected to a pulse-height threshold and coincidence test. The coincident events, shown by vertical lines in Figure 1-5(a), are tagged with the measured spectral difference defined as the uv signal minus the visible signal divided by the total uv plus visible signal. A histogram of the coincident events is stored in two buffers: a current buffer to which events are added in real time, and a past buffer composed of events that occurred in the recent past. The contents of the current buffer are periodically transferred to the past buffer, so long as the sensor does not go into alarm. When the sensor goes into alarm, the past buffer is not updated until the sensor goes out of alarm and then acquires enough events to fill a new current buffer. After turning on the sensor and during the acquisition of the first current buffer (1 min) it is assumed that no agent is present. Figure 1-5(b) shows a sample plot of the current buffer coincidence histogram. At regular temporal intervals the histogram of the current buffer events is decomposed, as seen in Figure 1-5(c), into a background component, an agent component, and an unknown component (not shown). The functional shape of the background component is taken to be the same as the past-buffer coincidence histogram. The functional shape of the agent component is given by a Gaussian with a central position and a standard deviation determined by previously acquired laboratory data for that agent, i.e., data such as shown in Figure 1-4. The unknown component is the remainder that the decomposition rou-

tine does not consider background or agent. When the agent signal component exceeds a preset threshold for a specified time duration (typically 30 s during the field trials) and the agent signal is greater than a specified fraction of the coincident signal (typically 30% during the field trials), the sensor declares an alarm condition, as seen in Figure 1-5(d). The sensor goes out of alarm when the agent signal goes below the threshold, or when the agent signal goes below the preset fraction of the coincident signal, and one of these conditions persists for a specified time duration.

The JFT-4 trials were conducted from 6 October to 6 November 1997 at Dugway Proving Grounds, Utah, about 75 miles southwest of Salt Lake City. These tests were conducted by the Army for the purpose of quantifying the performance of several different bioagent point detection technologies. The test site is a large, flat, high (4000 ft) desert environment with low (≤2 ft) vegetation. The tests were, with one exception, conducted at night, in order to take advantage of the generally more stable wind patterns. A total of 23 different scored trials were conducted consisting of 20 releases of *Bacillus subtilis* (a simulant for *Bacillus anthracis*, the causitive agent of anthrax) and three releases of *Erwinia herbicola* (a simulant for *Yersinia pestis*, the causative agent of the plague). There were no intentional releases of interferent aerosols during the trials, but occasionally aerosols from a nearby diesel generator or from vehicle motion drifted across the test site during trials. These unintentional interferents demonstrated the sensor's ability to discriminate agents from man-made interferents.

The test site was composed of five test stations equally spaced along a 52-m east-west line, as seen in Figure 1-6. Each test station was outfitted with conventional bacteria collection equipment, i.e., rotating slit air-to-agar samplers, for acquisition of "truth" data. This equipment was operated by the Army test site personnel. Because the truth samplers had to be incubated to grow and then count bacterial colonies, the truth data were not available in real time; in fact, they were only available to the test participants months after the trials were over. Participant test detectors were placed on either side of the test stations. We placed three bioaerosol fluorescence sensors on the test site: one immediately adjacent to test station 1, one midway between stations 2 and 3, and one midway between stations 4 and 5. The latter two sensors were not officially scored as part of the trials but they provided additional data for the purpose of analysis after the completion of the trials.

The bacterial aerosols were generated by agricultural sprayers mounted on the truck shown in Figure 1-6. The aerosols were released at about 800 m upwind of the line of stations. The aerosols were generally released at night and in wind conditions that would carry the aerosol cloud over the test site at right angles to the line of test stations. Sometimes the winds were highly variable, however, and the aerosol clouds might approach the test stations from unpredictable directions. For the purpose of evaluating the various tested technologies the bacterial aerosol releases were done at times unannounced to the test participants. At the end of each night of trials participants were required to deliver to the test director their sensor alarm on and off times.

A photograph of the bioaerosol fluorescence sensor at the JFT-4 trials is shown in Figure 1-7. The sensor is mounted on a tripod and has a black vertical 2-ft air-sampling tube, so that air intake is at the

6
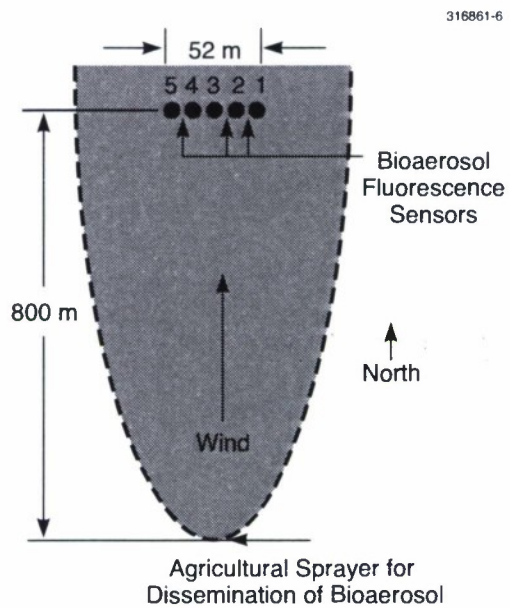
Figure 1-6. Layout of the JFT-4 field trials and photograph of bacteria dissemination truck showing four agricultural sprayers mounted on right-hand side of truck bed.
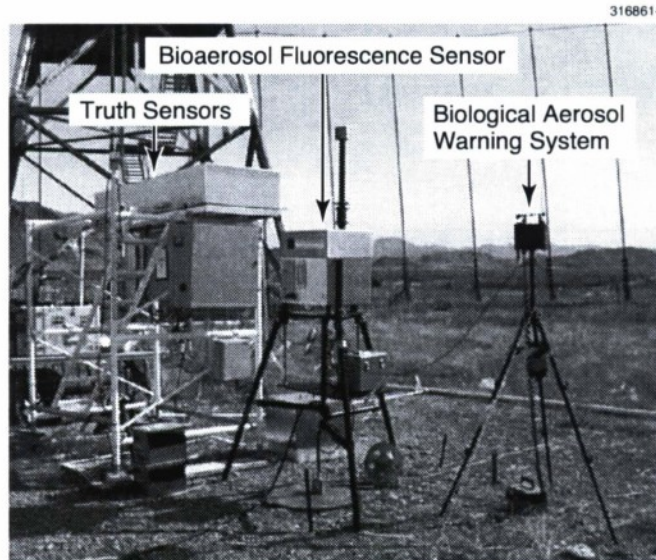
Figure 1-7. Bioaerosol fluorescence sensor located next to test station 1.

same height as the truth sensors. The truth sensors are mounted on the top of the white structure in the left of the photograph. At the time of this photograph the truth sensors were covered and cannot be individually seen. The sensor alarm declaration was sent via an RS232 cable to a radio transmitter housing the Biological Aerosol Warning System, a small tripod-mounted box on the right-hand side of the photograph.

Figure 1-8 shows the temporal behavior of the coincident signal as well as the decomposed agent signal for the east sensor during trial 8 on 27 October 1997. During the initial part of this trial the event rate is low; the histogram of events that occurred in this period is shown in the lower-left plot. About midway through the trial the coincident rate increases and the agent rate also increases. The initial rise in signal is followed by two smaller increases in the sensor signal. The histogram of events occurring during these periods is shown in the lower-right plot. As can be seen, the fraction of agent signal is much higher during the increased-event-rate periods as compared to early in the trial. The sensor went into alarm during the shaded periods in the upper plot.

Figure 1-9 shows the data from all three sensors on the test site during trial 22, as well as the truth data for comparison. We see from the truth data that the sensor declared alarms at the appropriate times during this test. Note that the sensors at different places in the grid measure similar, but by no means identical, signals. The truth data shown for the center of the grid is an average of the truth data from towers 2 and 3 on either side of our sensor placed between these towers. The truth data shown for the west end of the grid is an average of the data from towers 4 and 5 on either side of our sensor placed between these towers.

T. H. Jeys

8
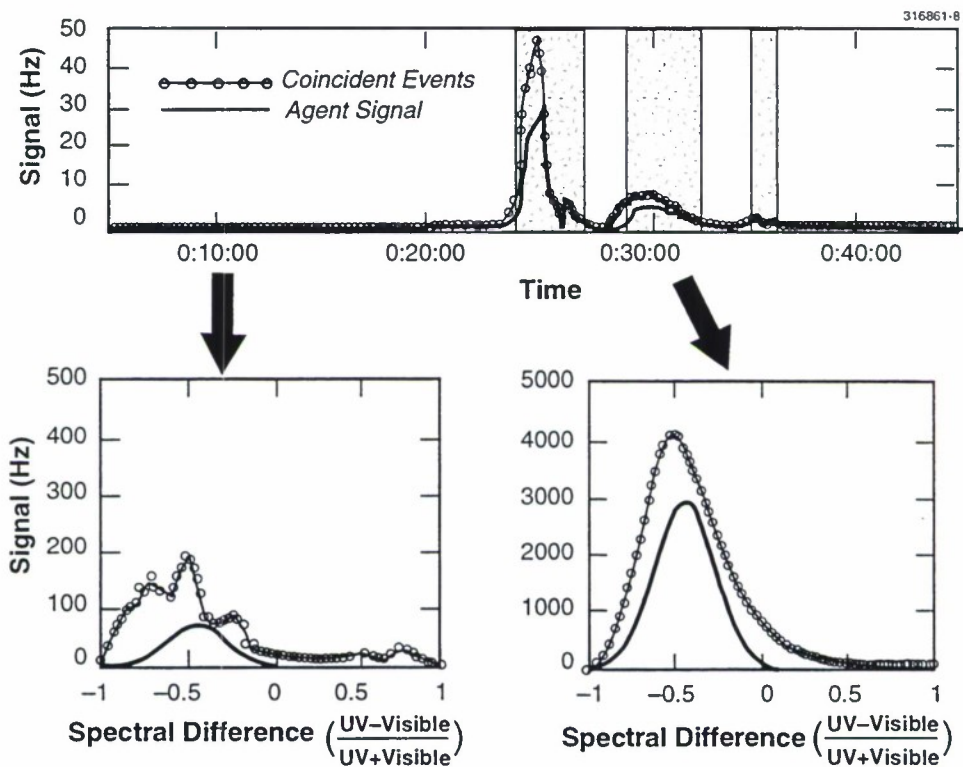
Figure 1-8. Data from sensor located next to test station 1 for trial 8.

REFERENCES

1.   Solid State Research Report, Lincoln Laboratory, MIT, 1998:1, p. 1.

2.   T. H. Jeys, presented at IRIS Conference, Tucson, Arizona, 5–7 March 1997.

3.   J. J. Zayhowski, *Laser Focus World* **32**, 73 (1996).

316861-9B
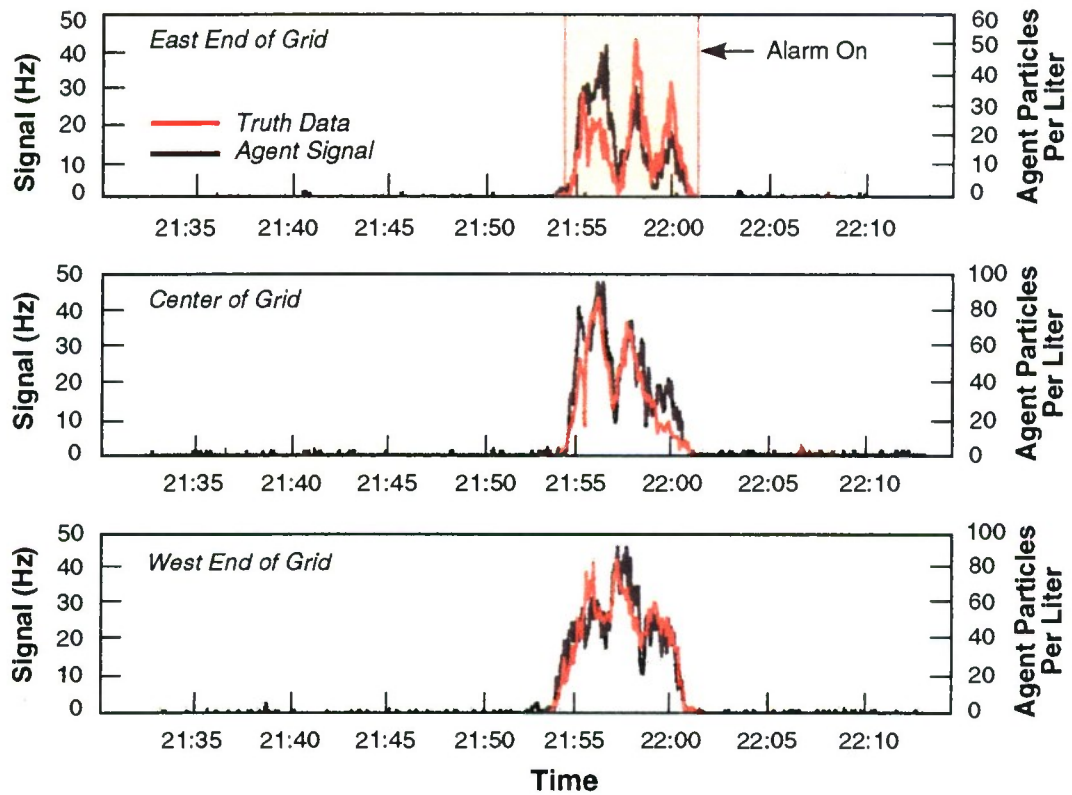
Figure 1-9. Sensor and truth data for all sensors during trial 22. As can be seen, the agreement is excellent.

10

2. ELECTRO-OPTICAL MATERIALS AND DEVICES

2.1 MICROWAVE LINKS USING EXTERNALLY MODULATED SEMICONDUCTOR LASER SOURCES

Laser sources for analog optical links have traditionally been diode-pumped Nd:YAG lasers at 1320 nm or distributed-feedback lasers coupled to erbium-doped fiber amplifiers at 1550 nm. Both of these types of laser source are large, expensive, and inefficient compared to using semiconductor laser oscillators and amplifiers exclusively. Although semiconductor laser oscillators are commercially available with low relative intensity noise (RIN) at frequencies below 1 GHz, their RIN at microwave frequencies can be high and their power output of 30 mW or less is inadequate for many link applications. We have developed a high-power, low-noise semiconductor laser amplifier [1] that addresses both of these problems. We have previously reported details of the performance of this amplifier, of a very quiet ($\approx$ −165 dB/Hz) Fabry-Perot (FP) diode laser oscillator using the same material, and of initial narrowband link measurements using these [2]. Here, we report more complete link measurements, including direct comparisons between the semiconductor and the Nd:YAG lasers.

We tested three different configurations of the laser source, as diagrammed in Figure 2-1. All the laser devices operated at 1320 nm. The key component we are evaluating in this paper is the tapered semiconductor amplifier, shown in Figure 2-2. It is made of InGaAsP/InP material grown by organometallic chemical vapor deposition. The device is a separate-confinement heterostructure, with three compressively strained quantum wells providing the gain. Light is coupled into a single-mode waveguide, which functions much like a typical semiconductor amplifier. The beam then expands by diffraction in the transverse direction of the tapered gain region. This expansion is necessary in order to achieve high saturated output power while keeping the current density and optical intensity at reasonable levels. The output beam is elliptical and astigmatic, but most of the power is still in the lowest-order mode and can be coupled to a fiber with appropriate optics.

316861-10
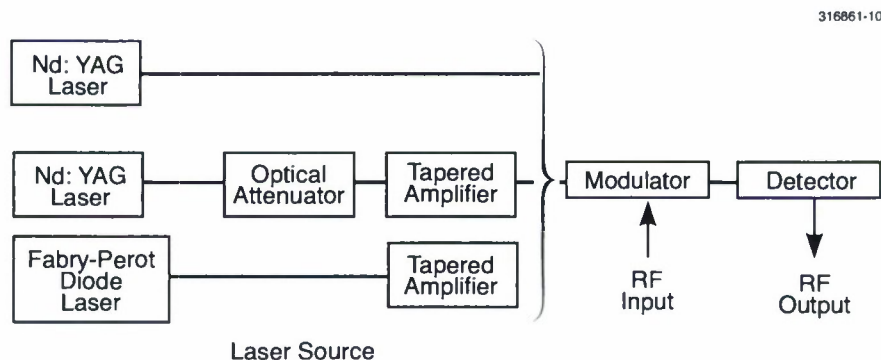
Figure 2-1. Block diagram of laser and link configurations measured.

11
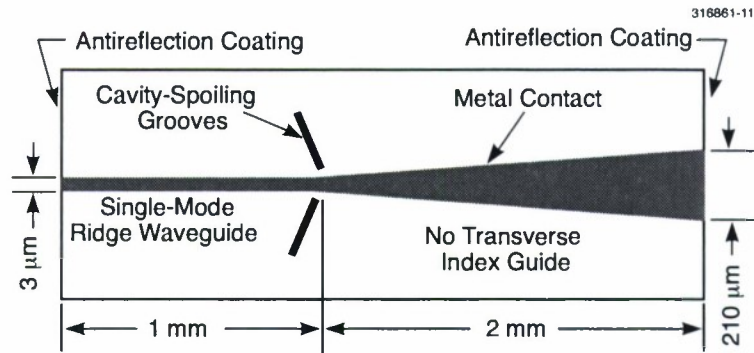
Figure 2-2. Top view of tapered semiconductor optical amplifier.

We coupled light into the input waveguide with a commercial isolated launcher, which gave about −2.2-dB fiber-to-waveguide coupling loss. The output coupling requires different lens properties (focal length and position) for the two different axes. For all the measurements here, we used a two-lens system, one microscope objective and one glass cylindrical lens, to collimate and circularize the beam, and a third lens to couple into the fiber. The best output coupling efficiency we achieved was −3.5 dB or 45%. (We have developed an anamorphic microlens made from GaP that can be attached to the amplifier output facet to circularize the beam and refocus it into a fiber. This should ultimately provide more efficient fiber coupling in a very small package.)

The small-signal fiber-to-fiber gain of this amplifier is about 30 dB at 2.0-A drive current, but the gain starts to depart from linear at about 50 mW of fiber-coupled output. The maximum output power levels we achieved were 820 mW in the beam and 240 mW in the fiber. For our link measurements here we set the amplifier to provide about 110 mW in the fiber, and then attenuated that further if needed.

The output RIN of the tapered amplifier is shown in Figure 2-3. It is $\leq$ −155 dB/Hz at frequencies $\geq$500 MHz for a range of operating conditions, and for either the semiconductor or the Nd:YAG oscillator. The lowest RIN at frequencies $\geq$500 MHz is achieved at 2.25-A drive current. Below 500 MHz, though, a lower amplifier drive current produces the lowest RIN. The RIN using the FP diode laser oscillator matches the RIN using the Nd:YAG laser oscillator fairly closely, when the amplifier's drive current and input power levels are kept the same. This is expected because the noise added by the amplifier is much larger than the amplified RIN of the FP diode. The exceptions to this are at low frequency, where the FP diode's RIN rises, and at 20 GHz. The rise near 20 GHz is probably associated with the FP diode's mode beat frequency, which is at 20.6 GHz.

The microwave links used all three laser sources shown in Figure 2-1. The modulator was a Mach-Zehnder modulator on lithium niobate with a velocity-matched traveling-wave electrode, built by UTP. Its V_π was 5.0 V at low frequency. The detector was an InGaAs *pin* diode built by Hughes to have

12
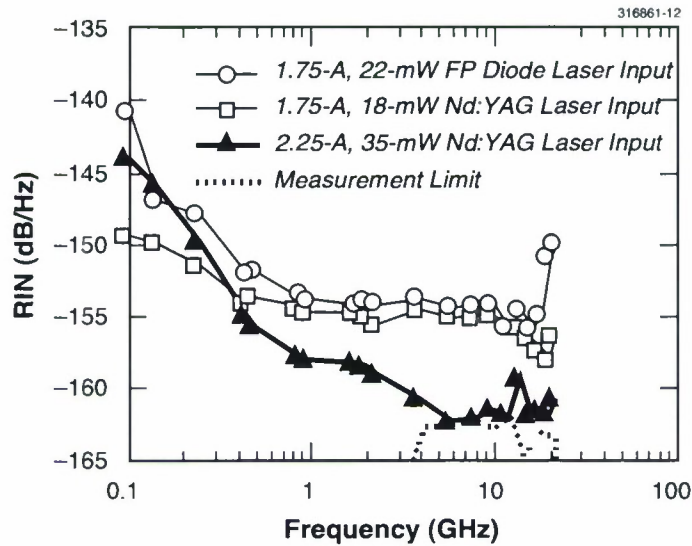
Figure 2-3. Relative intensity noise (RIN) of tapered amplifier with two laser oscillators. The legend gives the input optical powers and amplifier drive currents used.

good linearity at high photocurrent. Both devices were built for the TRP program [3],[4]. The modulator and detector responses, and the link gain (S_{21}) at the 90° modulator bias, are shown in Figure 2-4. The link's S_{21} is proportional to the sum of the modulator and detector responses.

The noise figure of the link with the three different lasers sources was measured, and the results are shown in Figure 2-5. At frequencies below about 12 GHz, the detector response is high enough that the primary noise source is shot noise or RIN. In this region the noise figure of the link is primarily determined by the modulator response, and so is fairly independent of frequency. At frequencies above 10 GHz the detector response has rolled off enough that receiver noise becomes significant. When receiver noise is significant, the link noise figure will rise as the link gain falls, which is what happens here above 12 GHz. These trends affect the results with all three laser sources.

The dynamic range is not affected by the modulator response because the modulator's input third-order intercept point and the link noise figure rise together as the modulator response falls. At very high frequencies, though, where the detector response has fallen enough that receiver thermal noise is reducing the noise figure, the dynamic range falls.

The detector can also affect the dynamic range by introducing its own nonlinearities. This detector, however, was very good in this regard; the measured third-order intercept points across frequency agreed very well with the intercept points predicted using the modulator nonlinearity alone. The detector performance was particularly impressive in the half-power bias case, where the average detector current was 8 mA and no impact of detector nonlinearity was evident.

13

316861-13
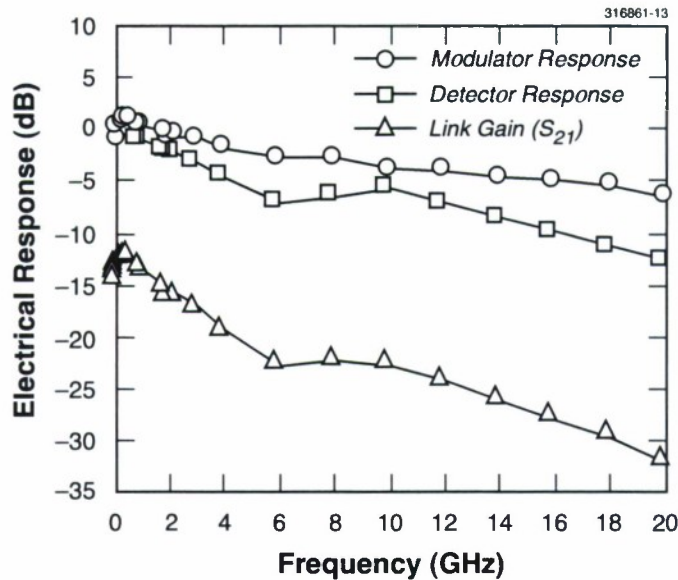
Figure 2-4. Frequency response of modulator and detector, and optical link gain.

Figures 2-5 and 2-6 show links in the suppressed bias condition, where the Mach-Zehnder modulator is biased toward its off states (128°–139°, or 12–19% transmission, was used here). This suppresses the optical carrier and thereby reduces the shot and RIN noise [2]. This technique is only useful on suboctave-bandwidth links, however, because it generates a large second-order distortion. Suppressed bias is particularly good at reducing the effects of RIN. In fact, the RIN of the link using the tapered amplifier at 2.25-A drive current is low enough that the suppressed bias condition is enough to make its performance nearly equal to the Nd:YAG-powered link at the higher microwave frequencies. The link using the all-semiconductor source, the FP diode oscillator with the tapered amplifier, still has enough RIN to give about a 5-dB penalty in noise figure. This penalty could be reduced by using an even lower transmission bias point, and by operating the tapered amplifier with a higher drive current. The differences in dynamic range between different laser sources are due mainly to differences in noise figure.

We also measured the links with the modulator set to the half-power point, 90° bias. This bias point is required for broadband links so that second-order distortion is suppressed. (For our links at 90° bias, the second-order dynamic range was measured to be the same as or larger than the third-order dynamic range at all frequencies.) In this case, the RIN from the tapered amplifier is significant, leading to a 5–8-dB penalty in noise figure over most of the band. This penalty would be smaller on a lower-performance link where less optical power reached the detector.
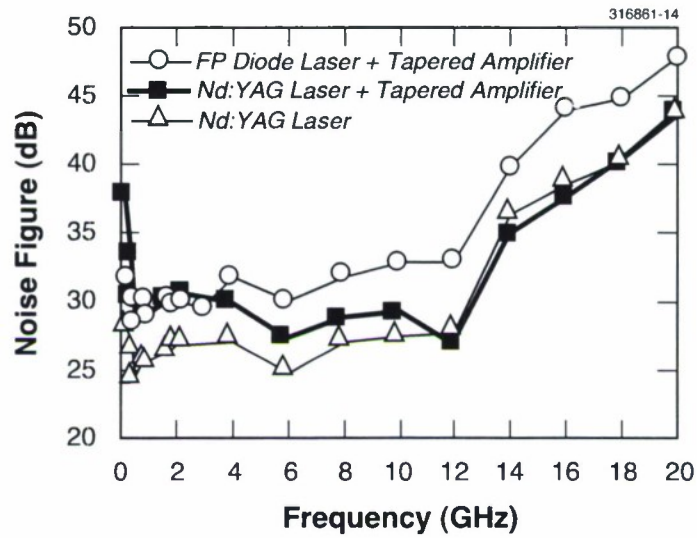
Figure 2-5. Noise figure of optical link, with three laser sources.
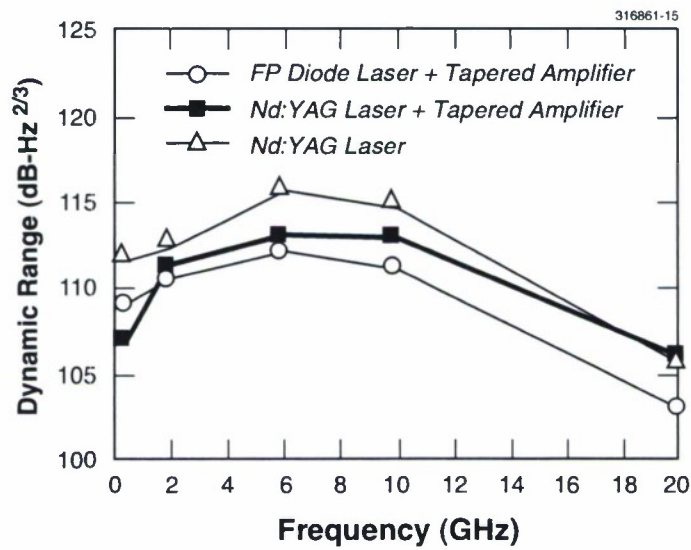
Figure 2-6. Third-order intermodulation-free dynamic range of optical link, with three laser sources.

15

Initial lifetime tests of 1300-nm tapered devices have been performed. We have run two tapered devices, one as an oscillator and one as an amplifier, for about 1000 h at 2.0-A drive current with no degradation in power or beam quality, at least to the ≈10% resolution of our experiment. We are expecting longer lifetimes for the 1300-nm devices than for 980-nm devices, similar to the trends for conventional single-mode lasers. However, longer tests with more devices are required to verify this.

Even at this early stage of development, the performance of the tapered amplifier makes it attractive for links in situations where the size, weight, and power consumption of the laser source are important. The noise figure and dynamic range of suboctave links using a laser source including a tapered amplifier are close to the noise figure and dynamic range of links using the traditional Nd:YAG laser. Further reductions in the amplifier's noise level would improve the performance of broadband links.

G. E. Betts   F. J. O'Donnell
J. P. Donnelly   J. N. Walpole
S. H. Groves   Z. L. Liau
L. J. Missaggia   R. J. Bailey
K. G. Ray   L. M. Johnson

2.2.   GaInAsSb/AlGaAsSb TAPERED LASERS EMITTING AT 2.05 μm WITH 0.6-W DIFFRACTION-LIMITED POWER

High-power, high-brightness sources in the mid-infrared wavelength region of 2–5 μm are very desirable for military applications such as infrared countermeasures. Strained quantum-well (QW) diode lasers consisting of GaInAsSb wells and AlGaAsSb barriers have exhibited excellent room-temperature performance near 2 μm, with threshold current densities J_{th} as low as 50 A/cm^2 [5], single-ended output power of more than 1 W cw from broad-stripe (100 m) lasers [5],[6], and quasi-cw power up to 4 W [7]. For high brightness, tapered lasers were previously fabricated in a GaInAsSb/AlGaAsSb QW wafer with J_{th} of 300 A/cm^2 [8], but the diffraction-limited power was limited to 120 mW. Here, we report much higher diffraction-limited power by the use of an improved wafer and better laser design.

The following single-QW laser structure was grown on a (100) n-GaSb substrate in a solid-source molecular beam epitaxy system with a valved As$_2$ cracking source and two conventional Sb$_4$ sources: 1.0-μm n^+-GaSb buffer, 0.1-μm n^+ graded region, 1.0-μm n-Al$_{0.9}$Ga$_{0.1}$As$_{0.07}$Sb$_{0.93}$ cladding, 50-nm n-graded region, 0.45-μm nominally undoped (p) Al$_{0.25}$Ga$_{0.75}$As$_{0.02}$Sb$_{0.98}$ barrier, 10-nm Ga$_{0.76}$In$_{0.22}$As$_{0.01}$Sb$_{0.99}$ well, 0.45-μm nominally undoped (p) Al$_{0.25}$Ga$_{0.75}$As$_{0.02}$Sb$_{0.98}$ barrier, 50-nm p graded region, 0.2-μm p-Al$_{0.9}$Ga$_{0.1}$As$_{0.07}$Sb$_{0.93}$ cladding, 0.8-μm p^+-Al$_{0.9}$Ga$_{0.1}$As$_{0.07}$Sb$_{0.93}$ cladding, 0.1-μm p^+ graded region, and 0.1-μm p^+-GaSb cap. 100-μm-wide broad-stripe lasers have exhibited room-temperature J_{th} as low as 50 A/cm^2 for a cavity length of 3 mm. From a standard analysis of differential quantum efficiency for different cavity lengths, the internal quantum efficiency and loss coefficient were determined to be 95% and 7 cm^{-1}, respectively. Output power of 1 W from a 100-μm aperture has been obtained under cw conditions at a heatsink temperature of 10°C.

16
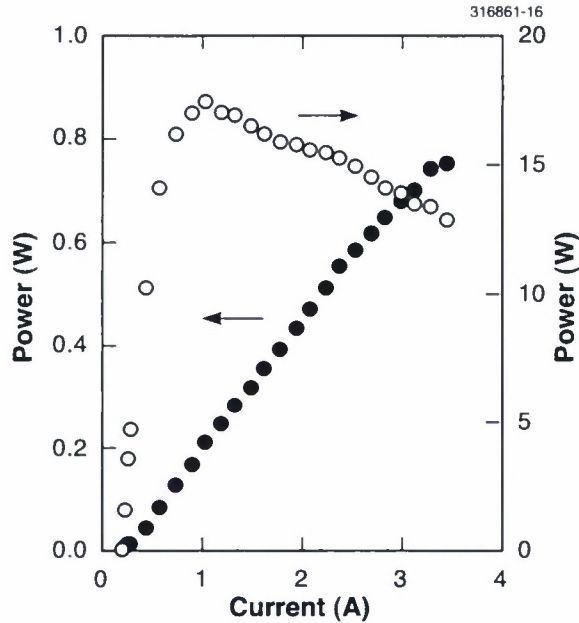
Figure 2-7. CW power vs current as well as power conversion efficiency of tapered laser at a heatsink temperature of 10°C. The ridge-waveguide section is 1 mm long and the tapered section is 1.4 mm long with a 140-μm aperture.

Figure 2-2 shows the schematic of a tapered laser. The beam from the ridge waveguide is allowed to diffract freely in the tapered section so that filamentation is suppressed. Cavity-spoiling grooves and low-reflection coating at the output facet suppress the FP oscillation. The long ridge-waveguide section (1 mm) provides a stable beam with sufficient intensity for efficient power extraction, and works as a filter to reject any higher-order spatial modes that are fed back from the tapered gain section. The length of the tapered section is 1.4 mm. The front and back facets were coated to have reflectivity <1% and 95%, respectively.

Figure 2-7 shows the cw output power vs current as well as power conversion efficiency at a heatsink temperature of 10°C. The threshold current is about 0.22 A and the initial slope efficiency is ~0.27 W/A, corresponding to a differential quantum efficiency of 44%. The maximum output power is 750 mW obtained at a current of 3.5 A. The maximum power conversion efficiency is 17.5% at an output power of 250 mW. For 2.2-mm-long broad-stripe lasers fabricated from the same wafer, the maximum power conversion efficiency was 22.5%.

The far-field pattern along the junction plane was measured under cw operation after removing the curvature of the phase. For this measurement, the heatsink temperature was 16.4°C. Figure 2-8 shows the far-field pattern at 3 A (600 mW), which was the maximum power level tested. The full width at half-maximum of the central lobe is 0.69°, which is 1× diffraction limited assuming a uniform 140-μm aperture.

0.69°

Far-Field Angle (deg)
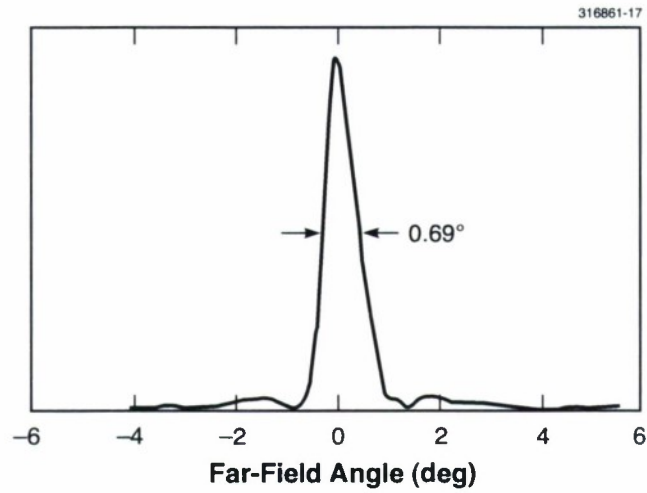
Figure 2-8. Far-field pattern of tapered laser at 3 A (600 mW cw). The heatsink temperature is 16.4°C. A diffraction-limited pattern is observed, with a full width at half-maximum of 0.69°, which is diffraction limited assuming a uniform 140-μm aperture.
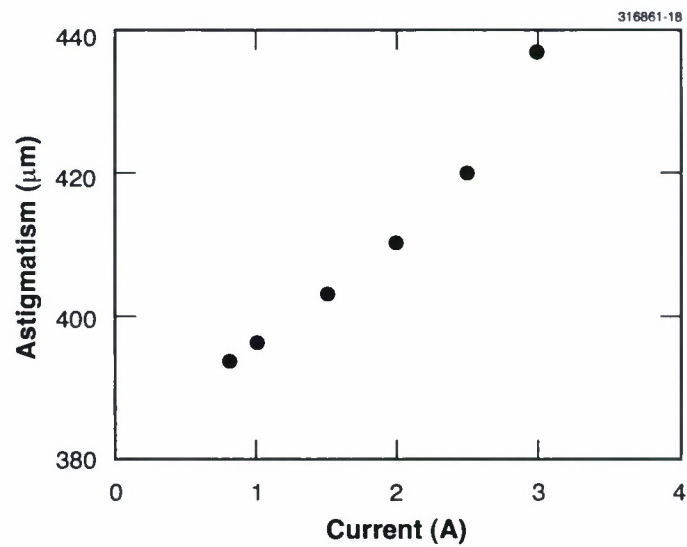
Current (A)

Figure 2-9. Astigmatism (measured from the output facet) of tapered laser in the lateral direction as a function of cw drive current.

18

The astigmatism of the tapered laser in the lateral direction as a function of cw drive current is shown in Figure 2-9. The focal point measured from the output facet changes from 392 μm at 0.75 A to 436 μm at 3 A, corresponding to a relative change of only about ±5%. This is comparable to the best values obtained for the InGaAs/AlGaAs tapered lasers emitting at ~0.98 μm.

H. K. Choi   M. K. Connors
J. N. Walpole   L. J. Missaggia
G. W. Turner   M. J. Manfra

REFERENCES

1. J. P. Donnelly, J. N. Walpole, G. E. Betts, S. H. Groves, J. D. Woodhouse, F. J. O'Donnell, L. J. Missaggia, R. J. Bailey, and A. Napoleone, *IEEE Photon. Technol. Lett.* **8**, 1450 (1996).

2. G. E. Betts, J. P. Donnelly, J. N. Walpole, S. H. Groves, F. J. O'Donnell, L. J. Missaggia, R. J. Bailey, and A. Napoleone, *IEEE Trans. Microwave Theory Tech.* **45**, 1280 (1997).

3. H. T. M. Wang, S. Thaniyavarn, P. Haugsjaa, C. M. Gee, W. J. Green, Jr., D. Sipes, C. H. Cox III, and S. A. Pappert, *Proceedings of the Seventh Annual DARPA Symposium on Photonics Systems for Antenna Applications* (1997), p. 155.

4. S. W. Merritt, J. P. Lin, E. Ackerman, H. V. Roussell, and B. Loo, *Proceedings of the Seventh Annual DARPA Symposium on Photonics Systems for Antenna Applications* (1997), p. 98.

5. G. W. Turner, H. K. Choi, and M. J. Manfra, *Appl. Phys. Lett.* **72**, 876 (1998).

6. D. Z. Garbuzov, R. U. Martinelli, H. Lee, P. K. York, R. J. Menna, J. C. Connolly, and S. Y. Naryan, *Appl. Phys. Lett.* **69**, 2006 (1996).

7. D. Z. Garbuzov, R. U. Martinelli, H. Lee, R. J. Menna, P. K. York, L. A. DiMarco, M. G. Matarese, S. Y. Naryan, and J. C. Connolly, *Appl. Phys. Lett.* **70**, 2931 (1997).

8. H. K. Choi, J. N. Walpole, G. W. Turner, S. J. Eglash, L. J. Missaggia, and M. K. Connors, *IEEE Photon. Technol. Lett.* **5**, 1117 (1993).

3. SUBMICROMETER TECHNOLOGY

3.1 LASER-FLUENCE AND MATERIAL-GRADE EFFECTS ON THE COMPACTION OF FUSED SILICA

Fused silica is the material of choice for optical elements in advanced lithography systems. However, despite its low initial absorption, even the best commercially available fused silica degrades when exposed to long-term low-fluence 193-nm laser irradiation. The degradation manifests itself through two major physical changes: color center formation and laser-induced densification or compaction [1]–[7]. Compaction alters the optical pathlength in an imaging system and thereby adversely affects its performance. Densification of glasses has been observed under irradiation by a variety of sources, dating back three decades: x-ray [8], gamma-ray [9],[10], electron [10]–[13], ion [14],[15], and neutron [10]–[16] irradiation. These studies indicate that the densification δ vs dose D can be expressed as

$$\delta = k(D)^x \tag{3.1}$$

where k and x are empirical constants with $x < 1$, over several decades of dose variation.

This report describes the experimental characterization of the effects of fluence and pulse count on laser-induced compaction in fused silica materials. This information is essential when designing accelerated lifetime testing experiments to qualify materials for use in 193-nm optical steppers.

The experimental exposure setup is shown in Figure 3-1. The laser is a Lambda Physik LPX 140, operated at 400 Hz in the constant energy mode (35 million pulses per day). With the aid of appropriate
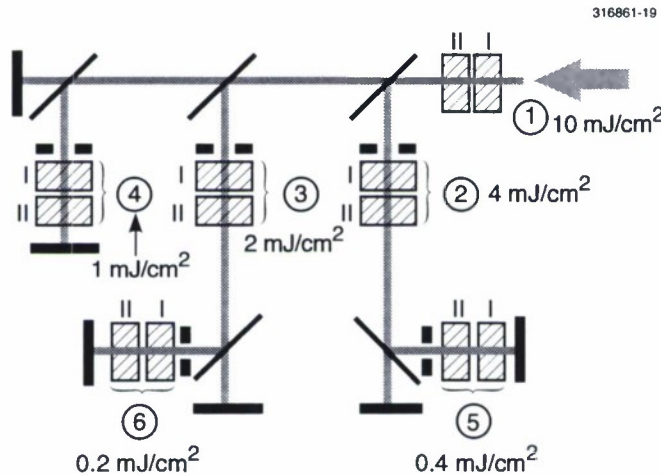
Figure 3-1. Experimental irradiation schematic. Fluences shown are nominal per pulse values. Roman numerals I and II refer to sample grades. Arabic numerals 1–6 next to the samples refer to station numbers.

beamsplitters several beam lines are formed, enabling the use of six sample stations, each at a different fluence. At each sample station two samples, one per grade, are irradiated. The fluence range incident on the first sample at each station spans 0.2–10 mJ/cm^2/pulse. We thus accomplish simultaneous irradiation of nominally identical samples of two grades of fused silica at fluences varying by a factor of 50×, with all samples experiencing the same nominal variations in laser performance. Such an arrangement permits the accurate determination of the scaling laws and their dependence on material grade.

The densification of fused silica samples is extracted from measurements of stress-induced birefringence by scanning light from a He-Ne laser beam across the excimer-irradiated spot, using a pair of crossed polarizers. In general, the densification is a function of irradiation geometry, such as the fraction of the sample being irradiated. In order to apply the information obtained from a specific experiment to other geometries, we compute the unconstrained densification [3]. This parameter is a geometry-independent quantity that is a function of only the material properties and the irradiation conditions.

The experiment lasted over 1.5 billion pulses. Because of the long duration of the experiment, extensive laser maintenance was required, involving replacement and realignment of the laser optics and replacement of the thyratron. These laser-maintenance activities resulted in variations of the incident laser intensity and pulse duration, as seen in Figure 3-2. These variations were accounted for in the dose calculation. We calculated the total two-photon effective dose for N pulses as

$$D_{\text{eff}}(N) = \int_0^N \frac{\Phi^2(N')}{\tau(N')} dN' \tag{3.2}$$

where Φ is the fluence per pulse and τ is the integral square pulse duration [17].

In Figures 3-3 and 3-4 the unconstrained densification is plotted vs effective dose for material grades I and II, respectively. The samples are labeled for each grade by station number, in accordance with the nomenclature of Figure 3-1. Note that the data presented in Figures 3-3 and 3-4 do not include those from the lowest and highest fluence stations (1 and 6, respectively). The samples exposed to the highest fluence (~10 mJ/cm^2/pulse) showed significant transmission degradation early in the experiment, and not enough data points were obtained for them. On the other hand, in the samples exposed to the lowest fluence (~0.1–0.2 mJ/cm^2/pulse), laser-induced stress birefringence remained on the order of the initial stress birefringence even after 1.6 billion pulses, and thus no reliable densification data could be extracted for them.

Our results indicate that an attempt to fit the measured compaction to Equation (3.1) results in different fits at different fluences and different grades, i.e., the k and x parameters are both fluence- and material-dependent. The variation of the k and x parameters vs average fluence Φ_{avg} for the two material grades is shown in Figure 3-5. At low fluences the x parameters of the two grades appear to converge, while the k parameter is different for each grade within the fit errors. A modest extrapolation to a fluence of 0.1 mJ/cm^2/pulse yields
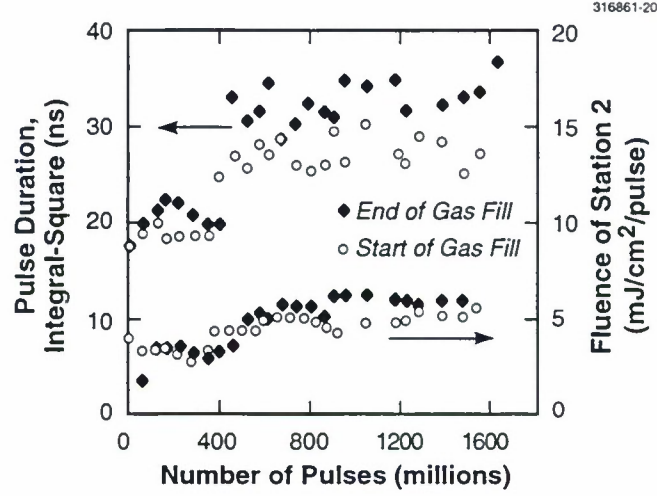
Figure 3-2. Double-Y plot of pulse duration and typical fluence variations (station 2) as a function of number of pulses irradiated. Data were collected at the beginning (open circles) and the end (dark diamonds) of each laser gas fill.

$$k = 0.43 \pm 0.01 \qquad x = 0.49 \pm 0.02 \text{ for grade I}$$

$$k = 0.34 \pm 0.1 \qquad x = 0.50 \pm 0.01 \text{ for grade II} \qquad (3.3)$$

The results presented in this paper represent a significant deviation from the suggested universality of the scaling law [17]. After careful analysis, we believe that our data unequivocally show that the exponential factor x and the preexponential coefficient k are indeed functions of fluence. We also conclude that the fluence dependence of k and x is often obscured by grade-to-grade and batch-to-batch material variations.

In order to propose an explanation of the fluence dependence of the k and x parameters, their physical significance must be understood. We attempt to relate these empirical parameters to more fundamental quantities governing the kinetics of densification. In this model a general nth-order kinetic equation is

$$\frac{d\delta}{dt} = G\dot{D} - R\delta^n \qquad (3.4)$$

where G and R are dose-independent generation and recombination rates, respectively, and $\dot{D} = \partial D/\partial t$ is the dose rate. For $n = 1$, this equation has the solution

23
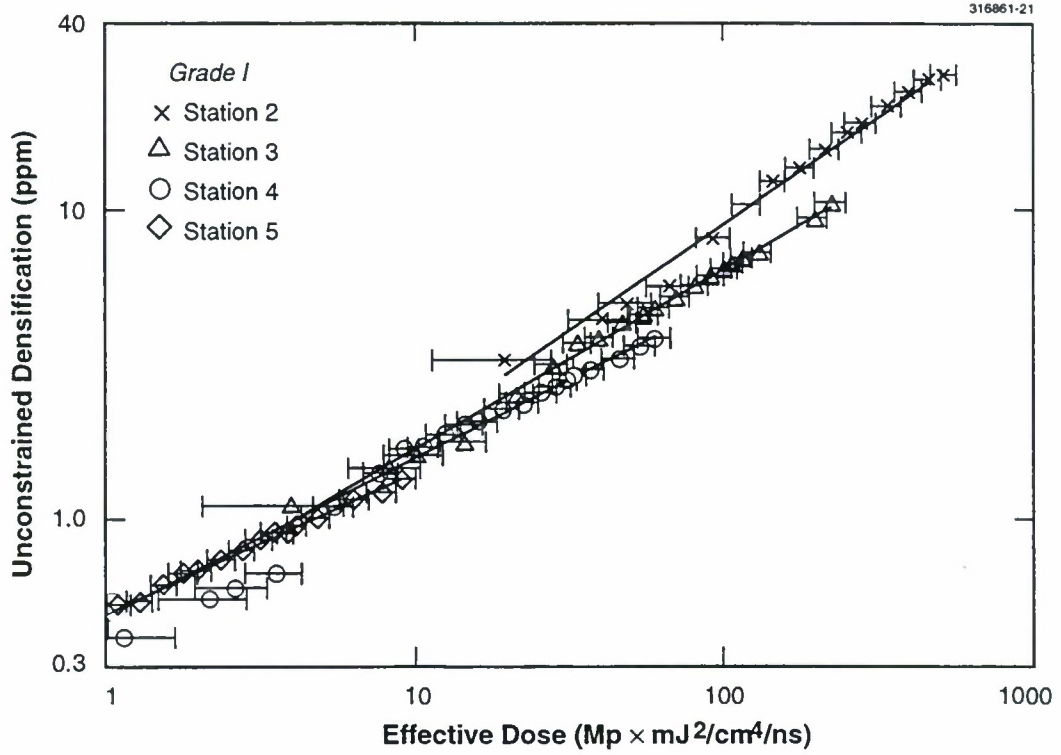
Figure 3-3. Unconstrained densification (ppm) vs effective dose for grade I samples, showing experimental data points with error bars, and power law fits.

$$\delta = \frac{G\dot{D}}{R}\left(1 - e^{-Rt}\right) \tag{3.5}$$

Griscom et al. [19] suggest that solutions to the power law equation (3.1) can be built from the series of saturating exponentials of the form of Equation (3.5), each with a set of dose-independent parameters G_i and R_i, i.e.,

$$\delta = \sum_i \frac{G_i\dot{D}}{R_i}\left(1 - e^{-R_i t}\right) \tag{3.6}$$

24
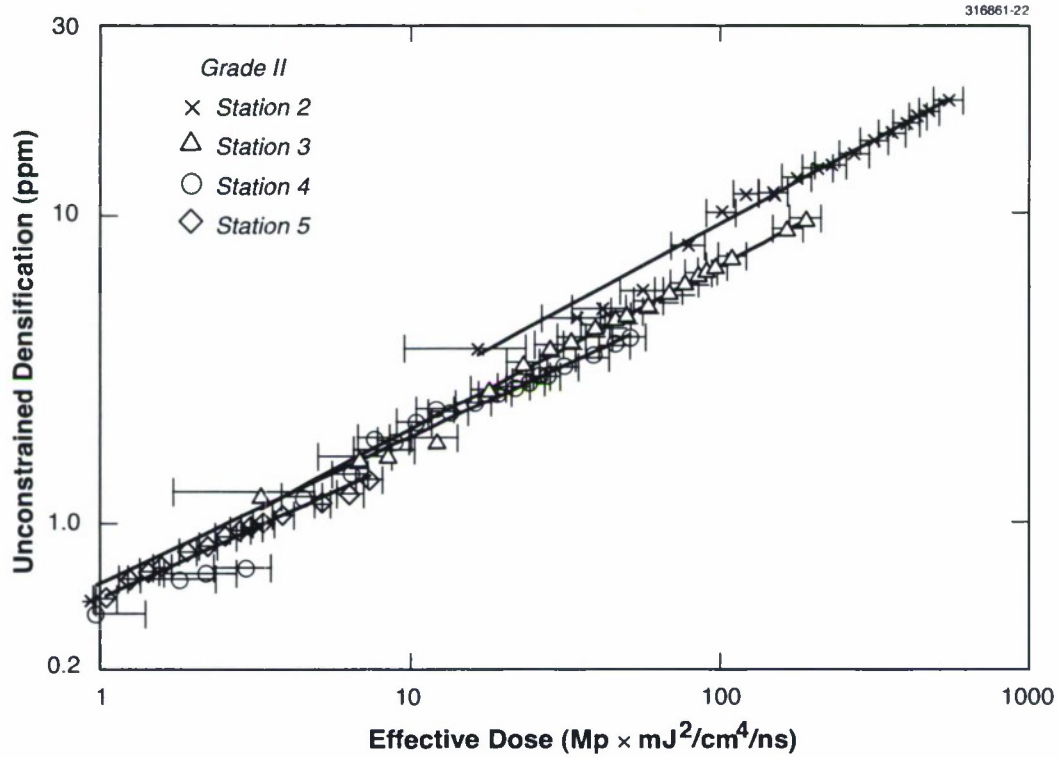
Figure 3-4. Unconstrained densification (ppm) vs effective dose for grade II samples tested, showing experimental data points with error bars, and power law fits.

The parameters are chosen as follows. First, for a given accumulated dose $D_{(i)}$, an approximation is made in which the *i*th component is assumed to saturate rapidly at $\delta_{(i)}$ and the other components do not significantly contribute to δ. From this approximation,

$$\delta_{(i)} = G_i D_{(i)} = k D_{(i)}{}^x \tag{3.7}$$

A second relation is obtained by differentiating Equation (3.1) with respect to *t* and setting the right sides of Equations (3.1) and (3.4) equal to each other. After rearranging, we obtain
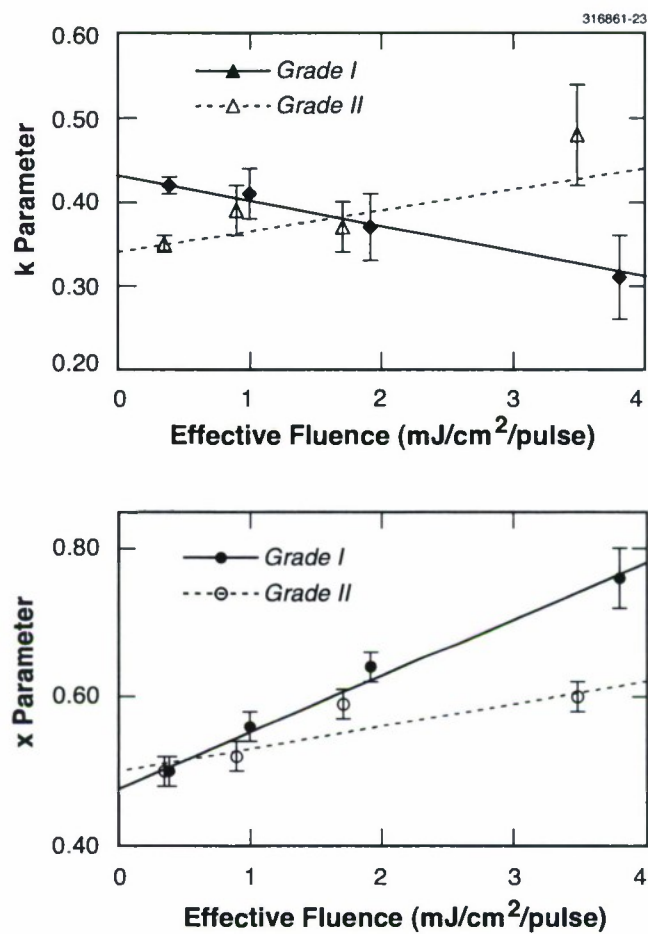
Figure 3-5. Fit results of data in Figures 3-3 and 3-4 to the power law of Equation (3.1). Error bars are fit errors. Straight lines are drawn to guide the eye.

$$G_i = kD_{(i)}{}^{x-1} \qquad\qquad (3.8)$$

and

$$R_i = (1-x)\frac{\dot{D}}{D_{(i)}} \qquad\qquad (3.9)$$

From our experience no relaxation of compaction is observed at or near room temperature in the dark. We postulate that both generation and recombination rates of compaction refer to light-induced fundamental excitonic processes that lead, respectively, to a decrease or an increase in the free lattice volume.

We present the results of a study of 193-nm laser-induced densification of fused silica, designed to understand the effects of fluence, pulse count, and material grade on the scaling of compaction. We fit compaction data as a function of dose to a power law. However, unlike previous work, we conclude that the fit parameters are themselves a function of the irradiation conditions, such as incident laser fluence. We relate the fit parameters of an empirical power law to recombination and generation rates of kinetic equations in an attempt to shed light on the fundamental processes of lattice rearrangement responsible for the densification.

V. Liberman   M. Rothschild
J. H. C. Sedlacek   R. S. Uttaro
A. Grenville

REFERENCES

1. M. Rothschild, D. J. Ehrlich, and D. C. Shaver, *Appl. Phys. Lett.* **55**, 1276 (1989).

2. M. Rothschild, *Opt. Photon. News* **5**, 8 (1993).

3. N. F. Borrelli, C. Smith, D. C. Allan, and T. P. Seward III, *J. Opt. Soc. Am. B* **14**, 1606 (1996).

4. C. Smith, N. F. Borrelli, D. C. Allan, and T. P. Seward, *Proc. SPIE* **3051**, 116 (1997).

5. D. C. Allan, C. Smith, N. F. Borrelli, and T. P. Seward III, *Opt. Lett.* **21**, 1960 (1996).

6. R. E. Schenker and W. G. Oldham, *J. Appl. Phys.* **82**, 1065 (1997).

7. F. Piao, R. Schenker, and W. G. Oldham, *Proc. SPIE* **3051**, 907 (1997).

8. W. Primak, *Radiat. Eff.* **45**, 29 (1979).

9. J. A. Ruller and E. J. Friebele, *J. Non-Cryst. Solids* **136**, 163 (1991).

10. W. Primak and R. Kampwirth, *J. Appl. Phys.* **39**, 5651 (1968).

11. C. B. Norris and E. P. EerNisse, *J. Appl. Phys.* **45**, 3876 (1974).

12. T. A. Deltin, D. A. Tichenor, and E. H. Barsis, *J. Appl. Phys.* **48**, 1131 (1977).

13. M. Rajaram, T. Tsung-Ein, and E. J. Friebele, *Adv. Ceram. Mater.* **3**, 598 (1988).

14. W. Primak, *J. Appl. Phys.* **43**, 2745 (1972).

15. E. P. EerNisse, *J. Appl. Phys.* **45**, 167 (1974).

16. R. A. B. Devine and M. Marchand, *Appl. Phys. Lett.* **63**, 619 (1993).

17. T. P. Duffey, T. Embree, T. Ishihara, R. Morton, W. N. Partlo, T. Watson, and R. Sandstrom, *Proc. SPIE* **3334**, 1014 (1998).

18. T. P. Seward III, C. Smith, N. F. Borrelli, and D. C. Allan, *J. Non-Cryst. Solids* **222**, 407 (1997).

19. D. L. Griscom, M. E. Gingerich, and E. J. Friebele, *IEEE Trans. Nucl. Sci.* **41**, 523 (1994).

4. HIGH SPEED ELECTRONICS

4.1 FIELD-EMITTER ARRAYS FOR INDUCTIVE OUTPUT AMPLIFIERS

Field-emitter arrays (FEAs) are desirable for use as cold cathodes for X-band inductive output amplifiers such as Klystrodes and twystrodes because they can provide advantages such as lower operating voltages, higher efficiency, and faster turn-on as compared to their thermionic counterparts. The ability to gate the beam at the source results in the elimination of the prebunching section of a traveling-wave tube, and a reduction in its overall length. However, rf vacuum microelectronics is one of the most demanding applications of field emitters, as the requirements include high current densities in relatively poor vacuum environments.

In the past we have fabricated molybdenum-tip FEAs with densities of 10^9 tips/cm^2 using holographic lithography. These devices produced high current densities (2400 A/cm^2) and dc current levels (up to 22 mA). Initial testing of such an FEA in a Klystrode yielded an output power of 2.5 mW (0.45 dBm) at 10.08 GHz, with an average beam current of 1.2 mA and a beam transmission ratio of greater than 98% [1].

Recently, the FEA process has been modified to take advantage of the fabrication facilities of the Microelectronics Laboratory (MEL). The fairly complicated holographic lithography has been replaced with more conventional 248-nm stepper lithography. The simplified MEL process reduces fabrication time to 4–6 weeks, and enables the incorporation of a variety of different array configurations on the same wafer, as shown by Figure 4-1. These single- and few-tip arrays were used to evaluate the stability and noise characteristics of the tips under dc test conditions. Typical emission current time data from a single tip is given in Figure 4-2. Average emitted currents are similar for 1-, 4-, 7-, and 9-tip devices, indicating that for these very small arrays, there is only one dominant emitting tip at any given time. The emission current and extracted noise characteristics for a 9-tip array are shown in Figure 4-3. The baseband noise characteristic is represented by a spectral density index γ, in which the power spectral density $S_{xx} \propto 1/f^\gamma$, and $S_{xx} = F[R_{xx}(\tau)]$. The noise index γ was extracted from low-frequency sampled time data, and calculated values of γ are all between 1 and 2, indicating that the noise appears to be caused by a combination of flicker and burst noise. Additionally, most of the noise power is concentrated at frequencies below 20 Hz (similar to results in [2]). This is advantageous for FEA use in microwave power tubes as it indicates that there will be very little broadening of, and low phase noise in, the 10-GHz carrier signal.

While the Klystrode test results demonstrated that the FEAs are microwave modulatable, their major drawback is premature failure due to arc currents, which is thought to be produced by ionization of gas molecules and/or desorbed contaminants. We are investigating two approaches to improve FEA lifetime. The first involves the incorporation of a resistive layer under the emitters to provide a series resistance at each tip [3], as is currently done by field-emission display manufacturers, as shown in Figure 4-4; the resistor acts as a current limiter and improves emission stability, as indicated in Figure 4-2, where an external emitter series resistor was used. However, the resulting high series resistance in combination with the gate
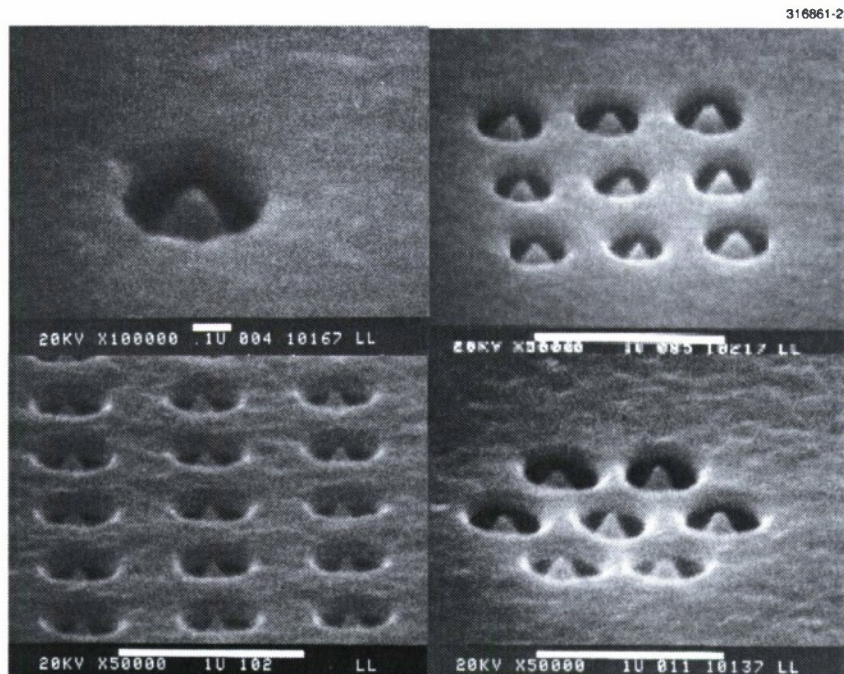
Figure 4-1. Scanning electron micrographs of field-emitter arrays (FEAs) with 1, 7, 9, and 100s of tips, all from the same substrate.

capacitance limits the frequency at which the gate-emitter voltage can be modulated, which is undesirable for rf applications. Fortunately, because the resistors under the tips are effectively in parallel, the total emitter series impedance of the array can be reduced by increasing the number of tips in the array. With proper design, the capacitance of the resistive layer can act as a bypass at X-band, while still providing enough resistance on a per-tip basis at lower frequencies to suppress arc currents. The effective emitter impedance of the array at X-band can thus be reduced to the order of a few ohms and still retain arc protection.

The reduction in emitter impedance can be illustrated with the following example. Assuming that the power from the arc will predominately be dissipated by melting of the gate metal, because the tip is in better thermal contact to the substrate than the gate, the power required to melt a gate volume typical of our FEAs is on the order of microwatts [4]. Therefore, in order to limit arc current at a gate operating voltage of 80 V, a minimum resistance of order 10^9 Ω/tip is required. This results in a maximum arc current of less than a microamp per tip. For such a tip, the impedance provided by the resistive layer under the tip is $z_i =$

Parameter	R_B = 1 kΩ	R_B = 100 kΩ	R_B = 1 MΩ
Mean x	6.2 μA	7.2 μA	4.5 μA
Standard Deviation σ	2.9 μA	3.1 μA	1.6 μA
Signal-to-Noise Ratio x/2σ	1.1	1.2	1.4
Noise Factor γ	1.7	1.9	1.7
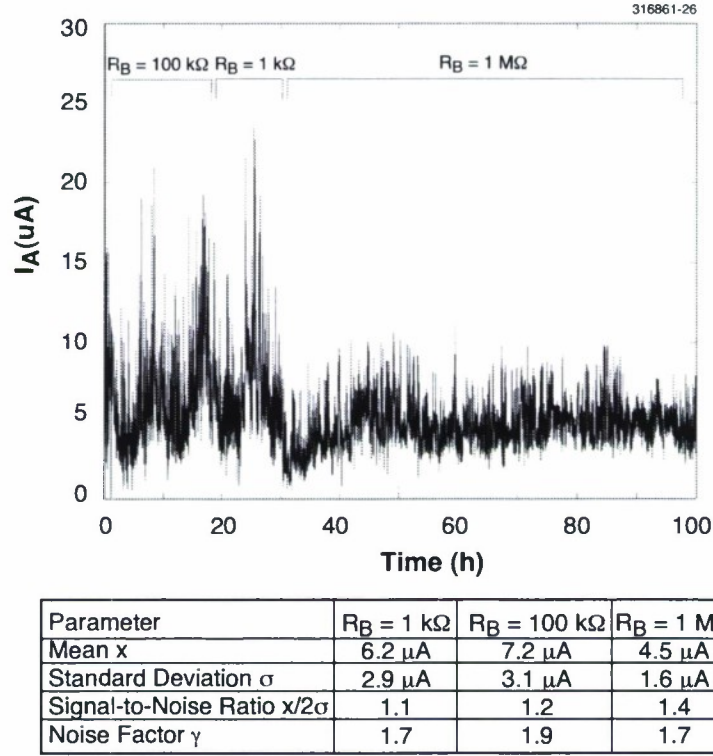
Figure 4-2. Emission current from single-tip array over four days, with varying emitter resistor R_B.

$R_i/(1 + j\omega R_i C_i)$, where $R_i = \rho t/A$ and $C_i = \varepsilon A/t$, and ρ, ε, t, and A are the resistivity, permittivity, thickness, and area of the resistive material under the tip, respectively. Therefore, the total impedance presented by an array of N tips is given by $z_E = z_i/N \cong t/(2\pi\varepsilon AN)$. For operation at high frequencies, we would like to limit z_E to less than a few ohms. The material properties and geometry of the resistive layer can be selected using the equation for z_E, based on the frequency of operation and the degree of current limiting desired. By way of example, an array with 70 300 tips of diameter 0.16 μm with a resistive layer of 500-Å thickness presents an impedance at 10 GHz of about 3 Ω.

The second protection approach, developed by NEC, is called the VECTL (VErtical CurrenT Limiter) [5] and is illustrated in Figure 4-5. This structure consists of groups of conventional molybdenum tips formed on top of silicon posts surrounded by oxide-filled trenches. Under normal operating conditions,

31
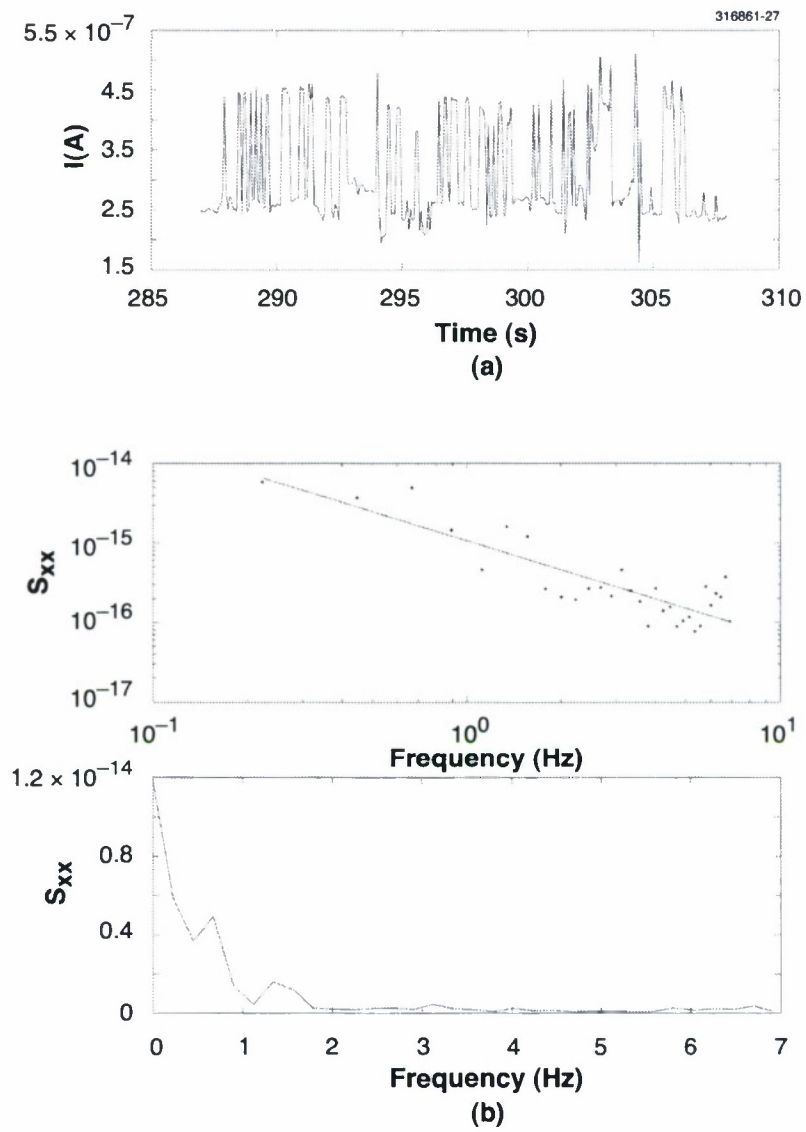
Figure 4-3. (a) Emission current and (b) calculated noise spectral density, both from a 9-tip array.

316861-28
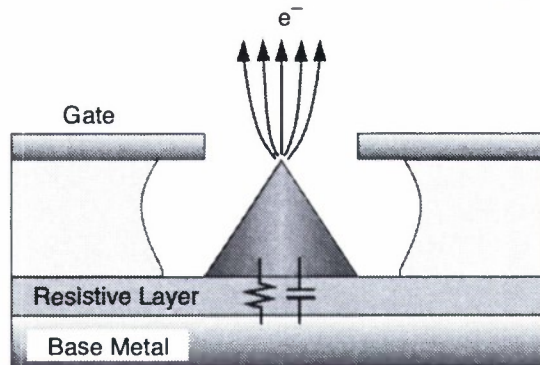
Figure 4-4. Arc-protected FEA using resistive layer.

316861-29

(a)

(b)

(c)
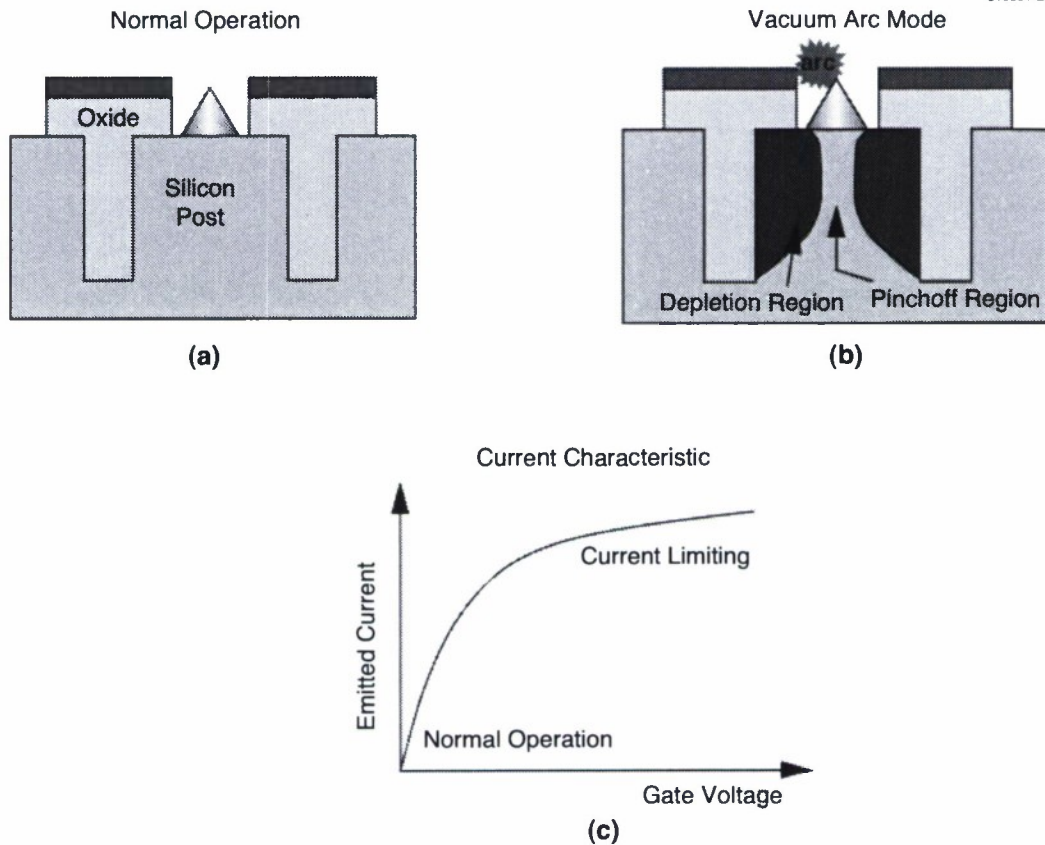
Figure 4-5. Arc-protected FEA using VECTL, showing (a) normal operation and (b) operation in vacuum arc mode with (c) current characteristic.

TABLE 4-1
Comparison of Performance of Current NEC Device and
Proposed Reduced Geometry Device

Parameter	NEC Device	Reduced Geometry Device
Device parameter		
Tip-to-tip spacing	1.2 μm	0.5 μm
Isolation trench width	1.5 μm	0.5 μm
Limiting current per pixel	200 μA	200 μA
Channel resistance per pixel	51 kΩ	20 kΩ
Gate capacitance per pixel	7 fF	2.2 fF
Calculated performance at 10 GHz		
Number of tips per quadrant	30 000	30 000
Annular outer diameter	900 μm	610 μm
Annular inner diameter	720 μm	526 μm
Cathode input impedance per quadrant	18 Ω	33 Ω
Peak current from four quadrants	120 mA	120 mA
Input power per quadrant	0.25 W	0.25 W
Beam modulation efficiency at 10 GHz (%) $\eta = (I_{max}-I_{min})/(I_{max})$	43%	87%

34

shown in Figure 4-5(a), the series resistance through the post to the tip is low, that is, orders of magnitude lower than that used in displays. The dimensions of the trench and post are set such that upon the application of a high voltage to the tip, as happens in a gate-to-tip arc, the silicon post under the affected tip will deplete, thereby pinching off the channel and limiting the current through the tip to a designed safe value, as seen in Figures 4-5(b) and 4-5(c). The structure then effectively acts like a junction field-effect transistor in saturation. Using the VECTL scheme, NEC has demonstrated cathode lifetimes of 5000 h in a tube environment, with dc emission. They have not, however, demonstrated rf gate modulation.

To evaluate the ability of the VECTL structure to provide rf current modulation, a simple analytical model, confirmed by simulations, was used. Two sets of geometries were compared, the existing design presented by NEC and a proposed design using a reduced geometry cathode, and Table 4-1 summarizes the results. Figure 4-6 is a simulation of current limiting in the proposed structure. The calculations indicate that a VECTL-based FEA has a much higher beam modulation efficiency at X-band if the tip dimensions are reduced and tip densities increased. Additionally, a narrower and thinner-walled beam can be obtained with the higher tip densities.

The VECTL approach offers a more robust alternative for arc protection than the very thin resistive layers, and additionally presents a low series resistance under normal operating conditions. An array of tips-on-posts would also have a reduced gate capacitance, as evidenced by the calculated higher beam transmission of the reduced geometry device.

L. Parameswaran   R. A. Murphy
M. A. Hollis   C. T. Harris
C. A. Graves

REFERENCES

1. R. A. Murphy, C. T. Harris, R. H. Mathews, C. A. Graves, M. A. Hollis, J. Shaw, M. A. Kodis, M. Garven, M. T. Ngo, K. L. Jensen, M. Green, J. Legarra, J. Atkinson, L. Garbini, and S. Bandy, *Proceedings of the International Conference on Plasma Science* (IEEE, Piscataway, N.J., 1997), p. 127.

2. J. T. Trujillo, A. G. Chakhovskoi, and C. E. Hunt, *J. Vac. Sci. Technol. B* **15**, 401 (1997).

3. C. Py and R. Baptist, *International Vacuum Microelectronics Conference Technical Digest* (IEEE, Piscataway, N.J., 1993), p. 23.

4. J. Shaw and H. Gray, *International Vacuum Microelectronics Conference Technical Digest* (IEEE, Piscataway, N.J., 1996), p. 547.

5. H. Takemura, Y. Tomihari, N. Furutake, F. Matsuno, M. Yoshiki, N. Takada, A. Okamoto, and S. Miyano, *International Electron Devices Meeting Technical Digest* (IEEE, Piscataway, N.J., 1997), p. 709.
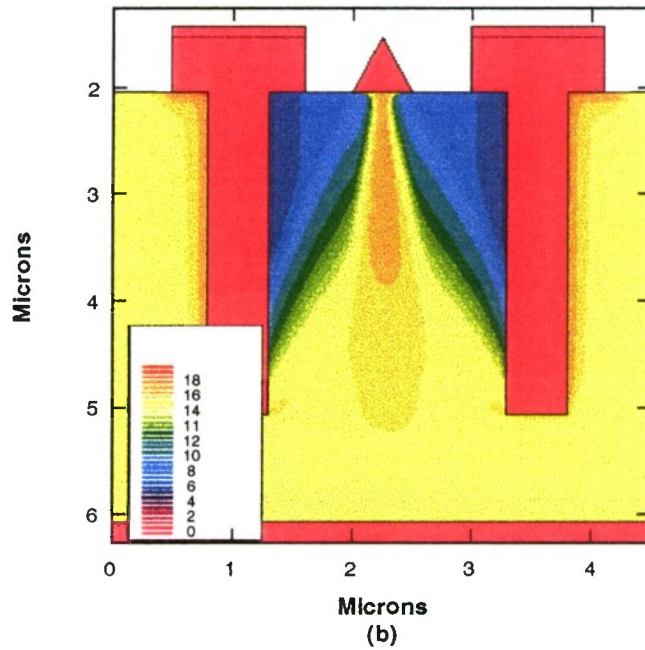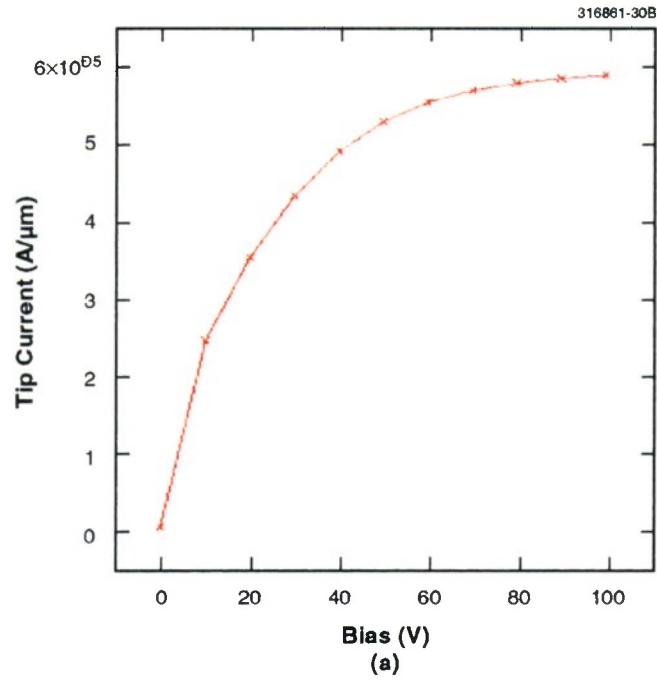
Figure 4-6. Simulation of VECTL current limiting using reduced geometry device: (a) tip current vs gate voltage under gate-to-tip arc conditions and (b) contour plot showing depletion regions at a gate/tip voltage of 100 V.

36

5. MICROELECTRONICS

5.1 IMPROVEMENTS IN THE UNIFORMITY OF LASER-ANNEALED BACK-SURFACE ILLUMINATED CCDs

Recent measurements of the response of back-surface illuminated charge-coupled devices (CCDs) across the visible revealed a spatial inhomogeneity, as seen in Figure 5-1(a), for a device illuminated with 410-nm wavelength light. This pattern, which resembles that of a brick wall, is most prominent in the blue or uv portions of the spectrum, but it extends across the visible into the red. The wavelength dependence of the inhomogeneity makes it difficult to distinguish from a fixed pattern. A line scan through the device indicates the nonuniformity is about 20%, peak to trough, as indicated in Figure 5-1(b).

The peak-to-trough contrast associated with this pattern has an Arrhenius dependence on temperature, with an activation energy measured at 0.12 eV. There is a known electron trap in Si that is 0.13 eV
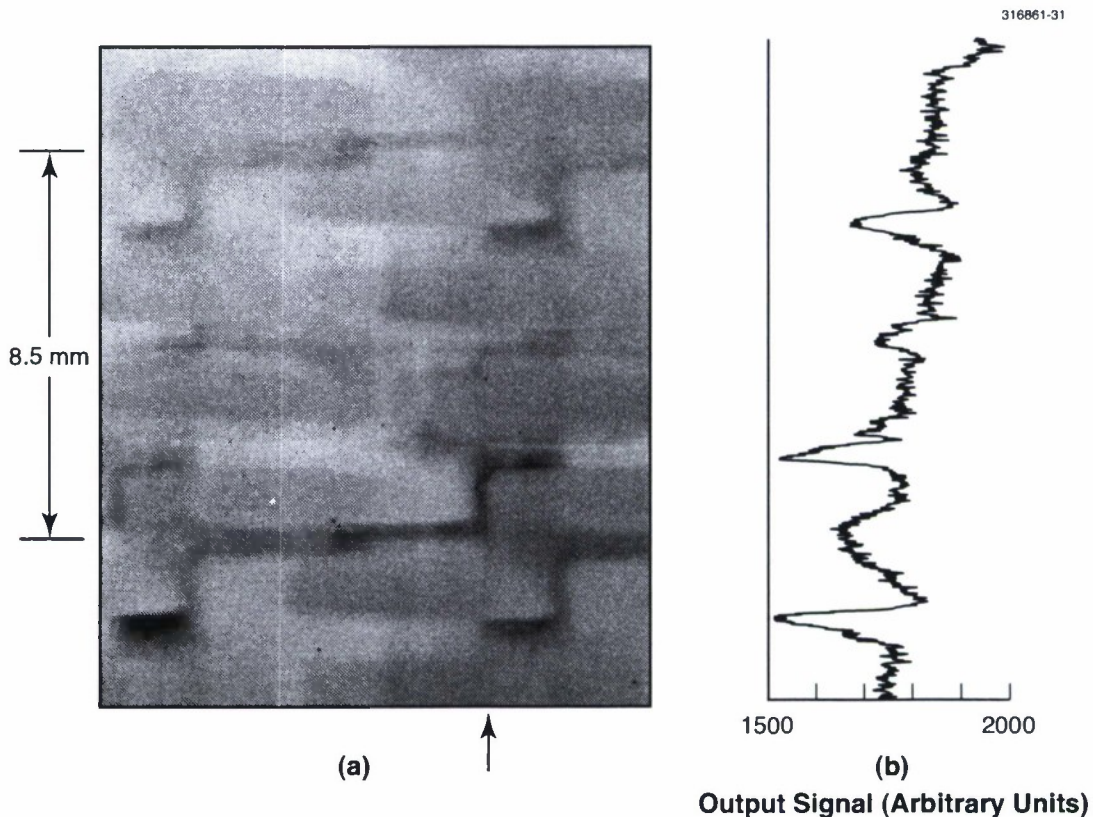
Figure 5-1. (a) Flat-field illumination of standard laser-annealed charge-coupled device (CCD) at −90 °C with 410-nm wavelength light. (b) Strength of output signal along vertical line trace indicated by arrow in (a).

37

316861-32

First-Layer Pulse

Slush Zone of Fourth-Layer Pulse

Unannealed Region Between Fourth-Layer Pulses
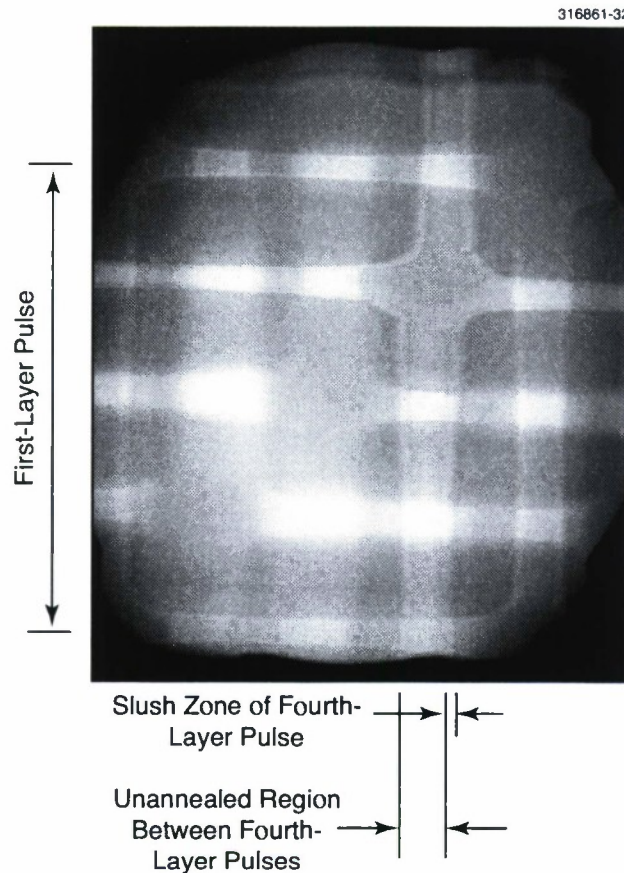
Figure 5-2. Brick wall pattern revealed by chemical etchant.

below the conduction band and is associated with B interstitials. Since it is necessary to have a large p^+ concentration on the back surface of the imager to drive photoelectrons towards the CCD buried channel, it is possible some of the B dopant atoms have not been incorporated in the Si lattice and can act as electron traps. Further evidence for a chemical basis for the defect is shown in Figure 5-2, where an implanted and laser-annealed surface has been subjected to a defect etch. In the scheme used for this sample, the surface was annealed with four different layers of laser pulses. The etchant reveals that the different layers have a similar chemical structure. Since the pulse layers overlap, the last layer has the most well-defined signature. It is evident the pulses within this fourth layer do not overlap and that each pulse is surrounded with a slush zone, a region where there is mixture of molten and solid Si during the laser pulse. If solid material remains within the liquid zone, there cannot be true epitaxial regrowth of the Si after laser annealing, leading to the possibility of defects associated with grain boundaries or incomplete activation of the B dopant atoms.

316861-33
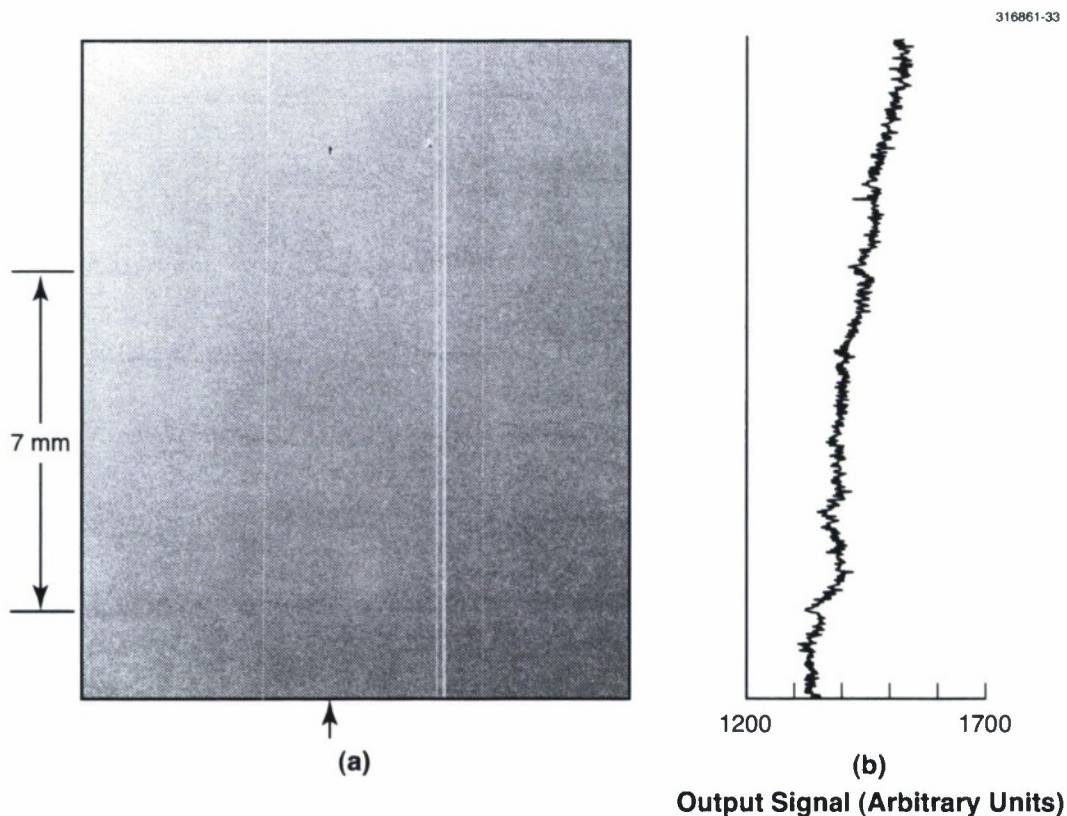
Figure 5-3. (a) Flat-field illumination of improved laser-annealed CCD at –90°C with 410-nm wavelength light. (b) Strength of output signal along vertical line trace indicated by arrow in (a).

To avoid these problems, three modifications were made to the laser anneal process: the implant dose was reduced, the laser pulse energy was reduced, and the degree of overlap of pulses within a given anneal layer was increased. The results of these changes are shown in Figure 5-3(a), where an illuminated CCD device shows little evidence of the brick wall pattern (the bright lines in the figure are due to an unrelated artifact). A line trace through this device is shown in Figure 5-3(b), where the peak-to-trough amplitude of the inhomogeneity is 2%. This data was obtained at low temperature and with short-wavelength light, corresponding to the conditions that produced the greatest nonuniformity for the old laser anneal process. Even though there must still be a slush zone or transitional region at the edge of a laser pulse, the uniformity of the device response is well within acceptable limits for the most demanding astronomical tasks.

J. A. Gregory
V. S. Dolat
A. H. Loomis

6. ANALOG DEVICE TECHNOLOGY

6.1 DEMONSTRATION OF ACCURATE YBa$_2$Cu$_3$O$_{7-\delta}$ CHIRP FILTERS ON BONDED-WAFER LSAT SUBSTRATES

Compressive receivers achieve the high sensitivity typical of a narrowband receiver while covering a wide instantaneous bandwidth by implementing an analog chirp-transform algorithm using chirp filters [1],[2]. High-temperature superconductive (HTS) chirp filters have allowed the instantaneous bandwidth of compressive receivers to be extended beyond 1 GHz [3]. This multigigahertz bandwidth coupled with new low-power digital post-transform pulse-processing electronics have enabled a receiver that can be realized with smaller size, weight, and power than competing technologies yet achieves the high performance demanded by electronic warfare applications [4]. An important milestone has been achieved with the demonstration of significantly more accurate 2.0-GHz-bandwidth 20-ns-long HTS chirp filters, fabricated on a new substrate material, lanthanum strontium aluminum tantalate (LSAT).

LSAT has a major advantage over LaAlO$_3$, the substrate most commonly used for microwave HTS applications. LaAlO$_3$ is plagued by structural twinning that causes the dielectric constant of the substrate to vary as much as a few percent, results in surface roughness on the substrate, and prevents optical substrate-thickness verification, as well as other complications. The variation of the dielectric constant is most significant since it prevents fabrication of high-accuracy chirp filters. LSAT is free from structural twinning and dielectric constant variation, as shown in Figure 6-1. Both LSAT and LaAlO$_3$ have the requisite chemical, thermal, and structural compatibility with HTS thin films, as well as relatively low microwave dielectric loss. Efforts continue to lower slightly the dielectric loss in LSAT to make it as low as that in LaAlO$_3$. The dielectric loss in LSAT at present is sufficiently low for HTS chirp filters as long as 40 ns.

The HTS chirp filters are based on a stripline configuration that uses two symmetrically placed ground planes on opposite sides of a pair of wafers. As a result, the packing density of the filter's tapped delay lines, and therefore the total chirp filter length, are directly proportional to the thickness of the two wafers. As the wafer thickness is reduced, a support wafer is required to prevent the thin wafer from breaking, particularly during HTS thin film growth. The technique used to bond a thin LSAT wafer to a thick LSAT wafer is diagrammed in Figure 6-2. The wafer-bonding process begins with a 250-μm-thick LSAT upper wafer with a sputtered layer of Hf/Au on the bottom surface and a 500-μm-thick LSAT base wafer with a sputtered layer of Hf/Au on the top surface. The wafers are forced together in a hot press, bonding the Au layers together. The Hf layers allow the Au to adhere to the LSAT. The bonded-wafer pair is then placed in a gas-pocket heater inside a cylindrical magnetron sputtering system, and the HTS material YBa$_2$Cu$_3$O$_{7-\delta}$ (YBCO) is grown as a thin film on the top surface of the thinner wafer [3]. Standard YBCO patterning techniques can be used following the YBCO growth. Future efforts will involve thinning the top wafer down to 125 μm to enable 40-ns chirp filters on 2-in.-diam LSAT substrates as was accomplished previously with LaAlO$_3$ [5].

316861-34
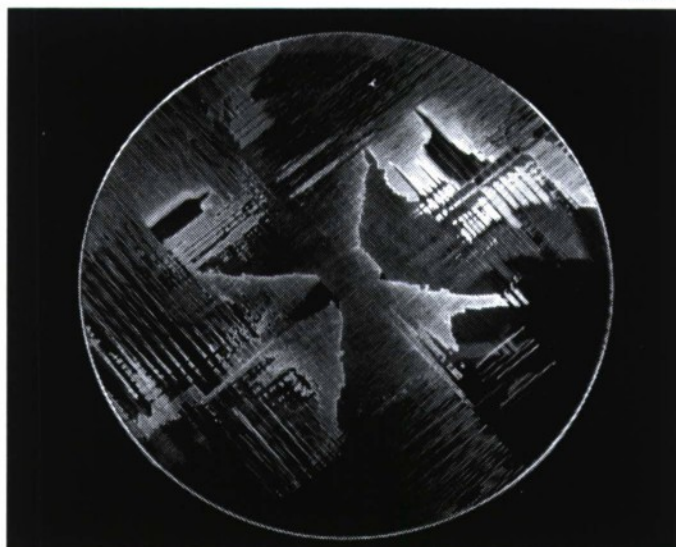
(a)
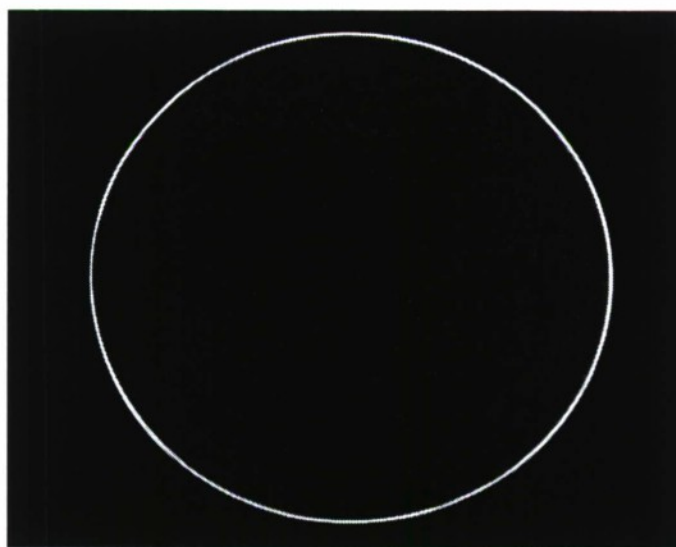
(b)

Figure 6-1. Photographs of 2-in.-diam substrates used for high-temperature superconductive (HTS) thin film growth: (a) LaAlO$_3$ highlighting the twinning structure characteristic of this material, and (b) LSAT highlighting the twin-free structure.
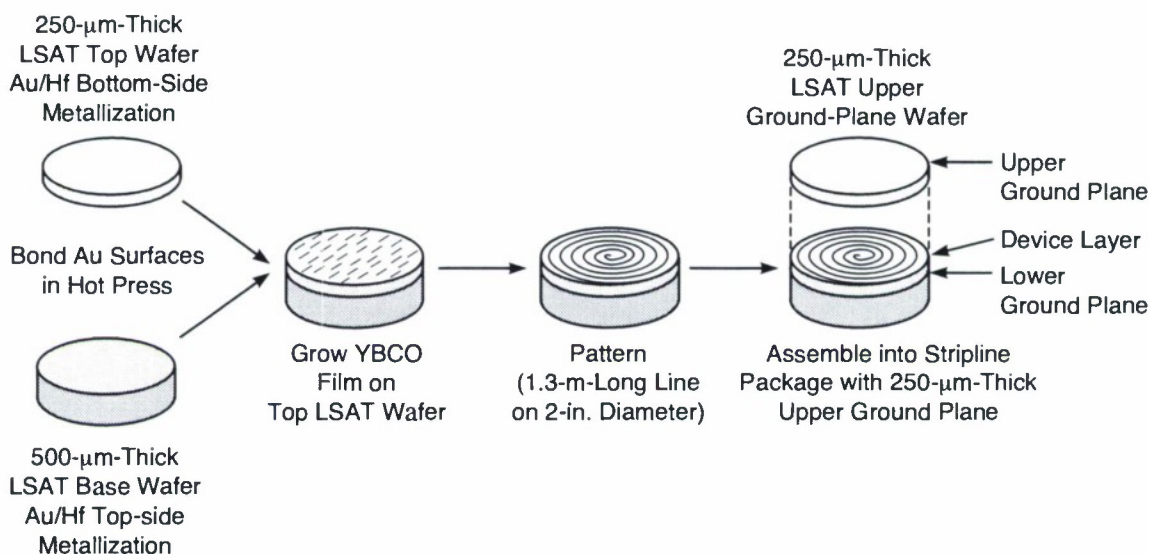
Figure 6-2. Illustration of wafer bonding technique used to fabricate 20-ns YBCO chirp filters on 250-μm-thick 2-in.-diam LSAT substrates. The chirp filters are assembled using tapped delay lines in a stripline structure, with a 250-μm-thick free-standing upper ground-plane wafer on top of the 250-μm-thick bonded device wafer.

A further step taken to improve accuracy, shown in Figure 6-2, involves the use of a free-standing (nonbonded) 250-μm-thick upper ground-plane substrate. This thin upper substrate can deform and reduce or eliminate the many air gaps between the two substrates in the stripline configuration. Air gaps also cause a variation in the effective dielectric constant for a stripline device and were identified as the dominant source of error in HTS chirp filters prior to this work.

The combination of LSAT substrates, with their uniform dielectric constant, and a thin deformable upper ground-plane substrate has resulted in the most accurate HTS chirp filters produced to date. Figure 6-3 shows the measured frequency response of a 2.0-GHz-bandwidth 20-ns-long Hamming-weighted HTS chirp filter made using YBCO on LSAT, as illustrated in Figure 6-2. Most notable is the small amplitude ripple in the transmission response of approximately 1 dB. The previous best result was on the order of 3 dB of amplitude ripple [4].

Another measure of the accuracy of a chirp filter is to operate the filter in a chirp-transform configuration in combination with a chirp generator, where the chirp generator produces a chirp signal more accurately than the chirp filter is able to compress that chirp signal into a compressed pulse [6],[7]. Paired echo theory quantifies how deviations from a linear chirp, particularly periodic deviations, in either the generated chirp signal or the matched chirp-filter compressor will result in "false" compressed-pulse mainlobes whose amplitude depends on the magnitude of the phase or amplitude deviations [8]. These false
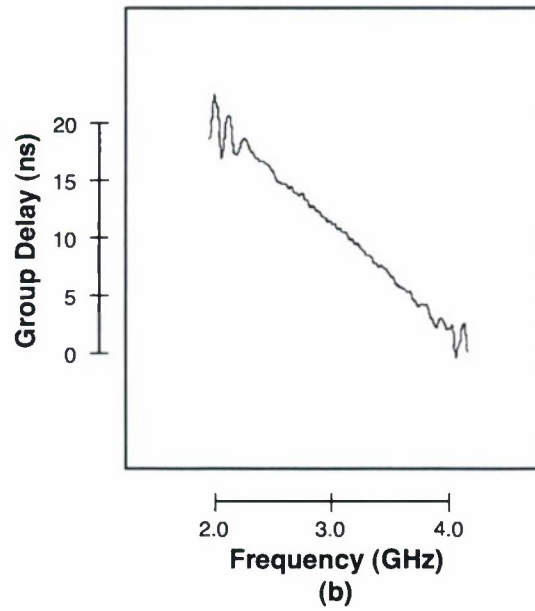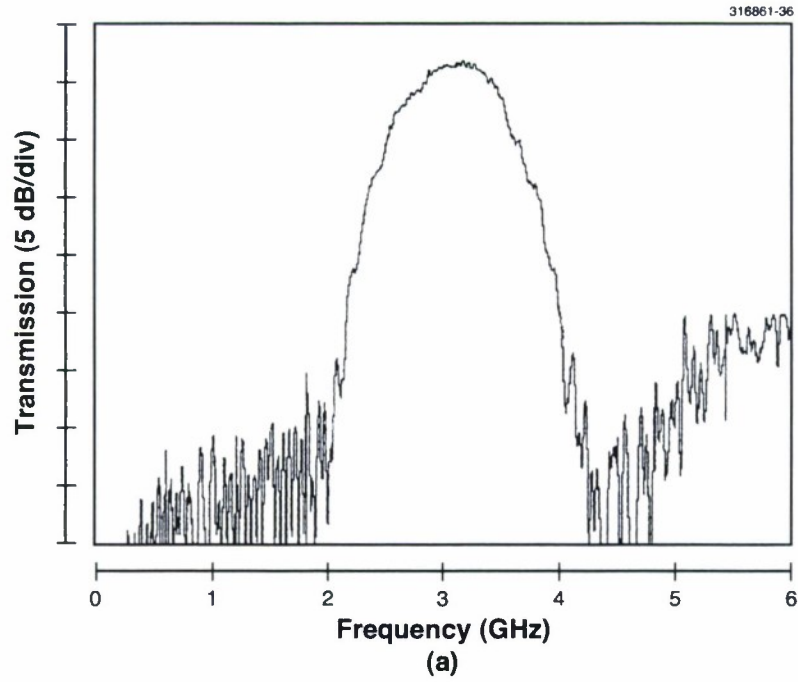
Figure 6-3. Measured frequency response of a 2.0-GHz-bandwidth 20-ns-long Hamming-weighted YBCO-on-LSAT chirp filter at 77 K: (a) transmission (S$_{21}$) vs frequency, and (b) group delay vs frequency measured using the downchirp ports of the filter.

mainlobes are termed error sidelobes and may appear above the ideal sidelobe levels set by weighting in the filter. For example, the first ideal sidelobe for Hamming weighting is −43 dB below the mainlobe. Error sidelobes −30 dB below the mainlobe indicate approximately 3% periodic phase and amplitude errors in the chirp-generator/chirp-filter combination. Error sidelobes −40 dB below the mainlobe require less than approximately 1% periodic phase and amplitude errors in the chirp-generator/chirp-filter combination.

Figure 6-4 shows the result of the operation of a linear chirp generator in combination with a 2.0-GHz-bandwidth 20-ns-long HTS chirp filter fabricated on LSAT. This chirp-generator/chirp-filter combination produced error sidelobes more than 30 dB below the mainlobe peak. Figure 6-4(a) shows the compressed pulse mainlobe (and error sidelobes) produced by a large-amplitude tone at 12.5 GHz. A second signal at 11.0 GHz, which was 30 dB smaller than the 12.5-GHz tone, was applied simultaneously. The 11.0-GHz signal was clearly detectable in the presence of the error sidelobes produced by the 12.5-GHz tone. Figure 6-4(b) shows only the mainlobe and error sidelobes from the large 12.5-GHz tone (the 11.0-GHz tone was turned off). The input signal frequencies for this demonstration spanned approximately 10–16 GHz, overscanning a wider input bandwidth at the expense of time coverage. The chirp generator swept from 12.5 to 20.5 GHz to produce an 8.0-GHz 80-ns-long chirp signal. The pulsewidth of the mainlobe of the compressed pulse was 0.67 ns. The 50-ns time window shown in Figure 6-4 represents 75 pulsewidths (66-MHz frequency resolution for a compressive receiver). The full analysis window was 91 pulsewidths long (61 ns) in this overscan mode covering an input bandwidth of 6.0 GHz.

The demonstration of error sidelobes more than 30 dB below the mainlobe peak is a significant achievement, and represents a 10-dB improvement over previous results using LaAlO₃ as a substrate material for the HTS chirp filters. Efforts under way now will result in 4.0-GHz-bandwidth 40-ns-long LSAT HTS chirp filters which, in combination with the chirp generator, should produce error sidelobes more than 40 dB below the mainlobe peak.

W. G. Lyons   R. L. Slattery
P. G. Murphy   D. J. Baker
A. C. Anderson   E. M. Macedo
R. R. Boisvert   J. C. Aversa
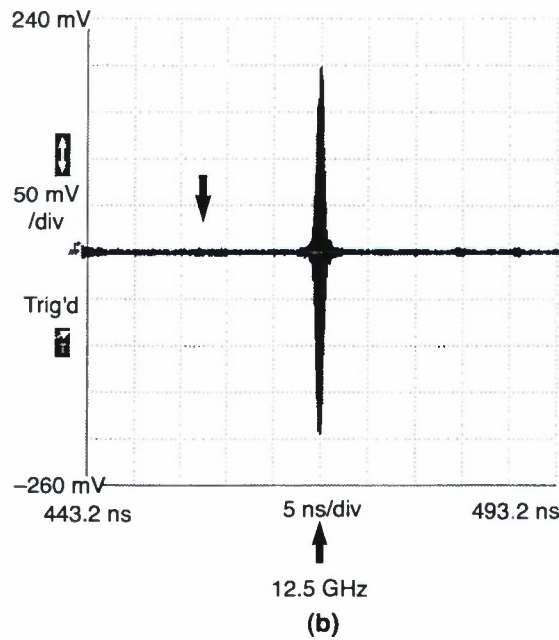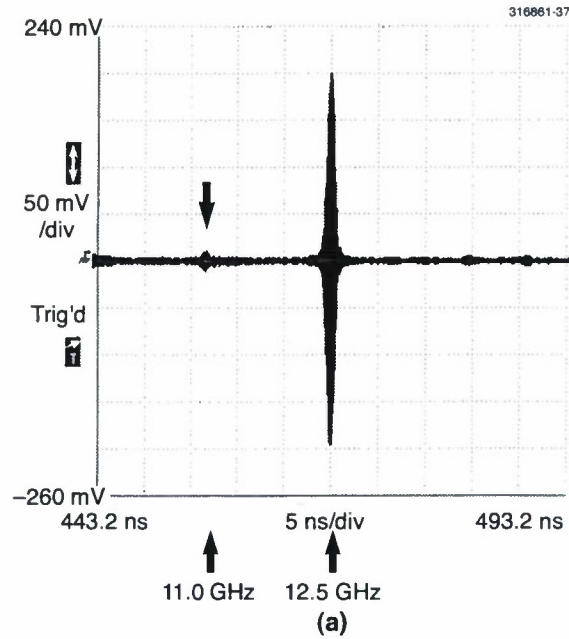
Figure 6-4. Compressed-pulse response of chirp-generator and LSAT HTS chirp-filter combination for a large-ampli-tude signal at 12.5 GHz with (a) small-amplitude signal (−30 dB down) turned on at 11.0 GHz, and (b) small-amplitude signal turned off. Error sidelobes produced in response to the large-amplitude signal are more than 30 dB below the mainlobe peak of the large-amplitude signal. The HTS chirp filter was operated at 77 K.

46

REFERENCES

1.   K. D. Breuer, J. S. Levy, and H. C. Paczkowski, *Microwave J.* **32** (10), 81 (1989).

2.   J. B.-Y. Tsui, *Microwave Receivers with Electronic Warfare Applications* (Krieger, Malibu, Fla., 1992).

3.   Solid State Research Report, Lincoln Laboratory, MIT, 1995:1, p. 41.

4.   W. G. Lyons, D. R. Arsenault, A. C. Anderson, T. C. L. G. Sollner, P. G. Murphy, M. M. Seaver, R. R. Boisvert, R. L. Slattery, and R. W. Ralston, *IEEE Trans. Microwave Theory Tech.* **44**, 1258 (1996).

5.   Solid State Research Report, Lincoln Laboratory, MIT, 1995:3, p. 41.

6.   P. J. Burke, *MTT-S International Microwave Symposium Digest* (IEEE, Piscataway, N.J., 1994), Vol. 2, p. 957.

7.   J. Levy, P. J. Burke, L. D. Cohen, and R. Cecchini, *MTT-S International Microwave Symposium Digest* (IEEE, Piscataway, N.J., 1993), Vol. 2, p. 1113.

8.   C. E. Cook and M. Bernfeld, *Radar Signals: An Introduction to Theory and Application* (Academic, New York, 1967).

7. ADVANCED SILICON TECHNOLOGY

7.1 INTEGRATED CCD/CMOS SILICON-ON-INSULATOR TECHNOLOGY

A low-power integrated charge-coupled device (CCD) and fully depleted silicon-on-insulator (FDSOI) process is being developed at Lincoln Laboratory. In this process, CCDs with high fill factor and quantum efficiency are fabricated with low-power digital CMOS circuits in a single SOI wafer. This approach retains high-performance CCD imaging while providing capabilities not yet available in the current scientific grade CCD imager process — fast, low-power CMOS digital circuits, analog circuits such as analog-to-digital converters, and low-voltage operation. Advantages of such a monolithic approach include enhanced electrical and thermal device isolation, increased CMOS device packing density, high-speed low-power CMOS without latchup, and potentially enhanced radiation performance in comparison to bulk devices.

A schematic diagram of the integrated approach is shown in Figure 7-1. As seen, the CCDs are fabricated in the substrate of a SOI wafer, and the CMOS transistors are built in the thin SOI. Since the present CCD process was designed for greater than 10-V operation and since the present 0.25-μm FDSOI CMOS process [1],[2] was designed for less than 2-V operation, significant modifications were made to the two technologies in order to achieve integrated operation at 3.3 V. Tables 7-1 and 7-2 compare the process
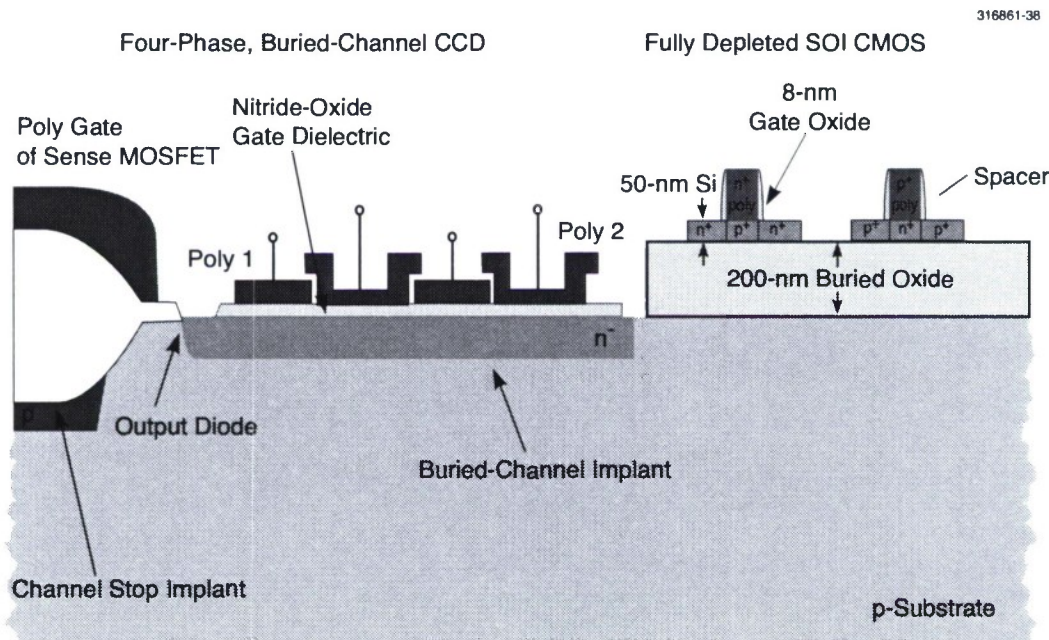
Figure 7-1. Schematic diagram of integrated CCD/CMOS design. For maximum charge collection, CCDs are fabricated in the bulk silicon-on-insulator (SOI) handle wafer, and for low-power fully depleted operation, CMOS circuits are fabricated in the thin SOI layer.

49

TABLE 7-1
Integrated CCD/Fully Depleted Silicon-on-Insulator CMOS Process
Parameters: Material and Dielectrics

	Standard Process	Integrated Process
Starting material	CMOS: SIMOX CCD: Bulk Si	Bonded SOI wafers
Bulk resistivity	CCD: 300 Ω cm or higher	Same
SOI silicon thickness	CMOS: 50 nm at completion, 60 nm at start	Same
SOI buried-oxide thickness	200 nm	Same
Isolation technology	CMOS: mesa etched CCD: LOCOS field oxide	Same
CCD gate dielectric	15-nm PECVD SiO_2 + 40-nm Si_3N_4 + 60-nm SiO_2	10-nm PECVD SiO_2 + 20-nm Si_3N_4 + 30-nm SiO_2
SOI CMOS gate oxide	8-nm SiO_2	Same
CCD area field oxide	500 nm	250 nm
CCD interpoly oxide	200 nm (wet)	100 nm (dry)
*Deposited oxide metal 1/poly	CMOS: 450-nm LTO (minimum)	450-nm LTO (minimum)
*ILD metal 2/metal 1, where metal 1 is over poly	CMOS: 600-nm PECVD TEOS oxide	600-nm PECVD TEOS oxide

*Interlevel dielectric (ILD) and poly/metal 1 oxides are planarized, which results in a layout-dependent thickness distribution.
 LTO = low-temperature oxide.

TABLE 7-2
Integrated CCD/Fully Depleted Silicon-on-Insulator CMOS Process
Parameters: Conductors

	Standard Process	Integrated Process
Poly 1	CCD: In-situ doped n^+	Same
Poly 1 thickness	CCD: 430 nm	250 nm
Poly 2	CMOS: Complementarily implanted As or BF_2 CCD: In-situ doped n^+	Complementarily implanted P, As, or BF_2
Poly 2 thickness	CCD: 400 nm CMOS: 225 nm	225 nm
Metal 1 and 2	CMOS: Ti : AlSi : Ti : TiN CCD: Al, metal 1 only	Ti : AlSi : Ti : TiN
Metal 1 and 2 thicknesses	CMOS: 630 nm = 40 : 500 : 40 : 50 nm CCD: 1.1 μm, metal 1 only	Same as CMOS
Metal 3	CMOS: Ti : AlSi : Ti	Same
Metal 3 thickness	CMOS: 580 nm = 40 : 500 : 40 nm	Same
Plug metal	CMOS: Ti : TiN : Ti : AlSi	Same
Plug metal thickness	CMOS: 760 nm = 30 : 100 : 30 : 600 nm	Same
Poly 3	CCD: In-situ doped n^+	None
Poly 3 thickness	CCD: 330 nm	None

parameters used in the low-voltage (3.3 V) integrated CCD/SOI-CMOS process to those used in the nonintegrated standard high-voltage CCD (>10 V) and FDSOI CMOS (<2 V) processes. The low-power CCD process employs thinner dielectrics and sharper doping profiles to maintain charge-handling capacity while the CMOS process employs slightly longer channel lengths and modified doping profiles to offset parasitic effects. The CCD process also benefits from the deep-uv lithography and three-level fully planarized metal [3] already in use for 0.25-μm FDSOI CMOS fabrication.

Table 7-3 compares the simulated performance of the new integrated 3.3-V process to that of the standard CCD and FDSOI processes. Simulations confirm that the modification of dielectric thickness and implant profile is sufficient to achieve high CCD well capacity at 3.3 V. Figure 7-2 illustrates the simulated potential profile for four-phase CCD operation. Note that the potential well is confined under the 3.3-V

TABLE 7-3
Integrated CCD/Fully Depleted Silicon-on-Insulator CMOS
Performance Parameters

	Standard Process	Simulated Integrated Process
CCD clock swing	10 V	3.3 V
CCD gate dielectric	15-nm PECVD SiO_2 + 40-nm Si_3N_4 + 60-nm SiO_2	10-nm PECVD SiO_2 + 20-nm Si_3N_4 + 30-nm SiO_2
Buried-channel implant	P, 200 keV, 1.25×10^{12} cm^{-2}	P, 125 keV, 1.25×10^{12} cm^{-2}
Charge capacity	10^{12} cm^{-2}	5.3×10^{11} cm^{-2}
Bulk enhancement mode n-MOS V_{th}	N/A	0.30 V
Bulk depletion mode n-MOS V_{th}	−5 V	−3 V
SOI CMOS operating voltage	2.0 V	3.3 V
n-MOS threshold voltage	0.40 V	0.40 V
p-MOS threshold voltage	−0.40 V	−0.40 V
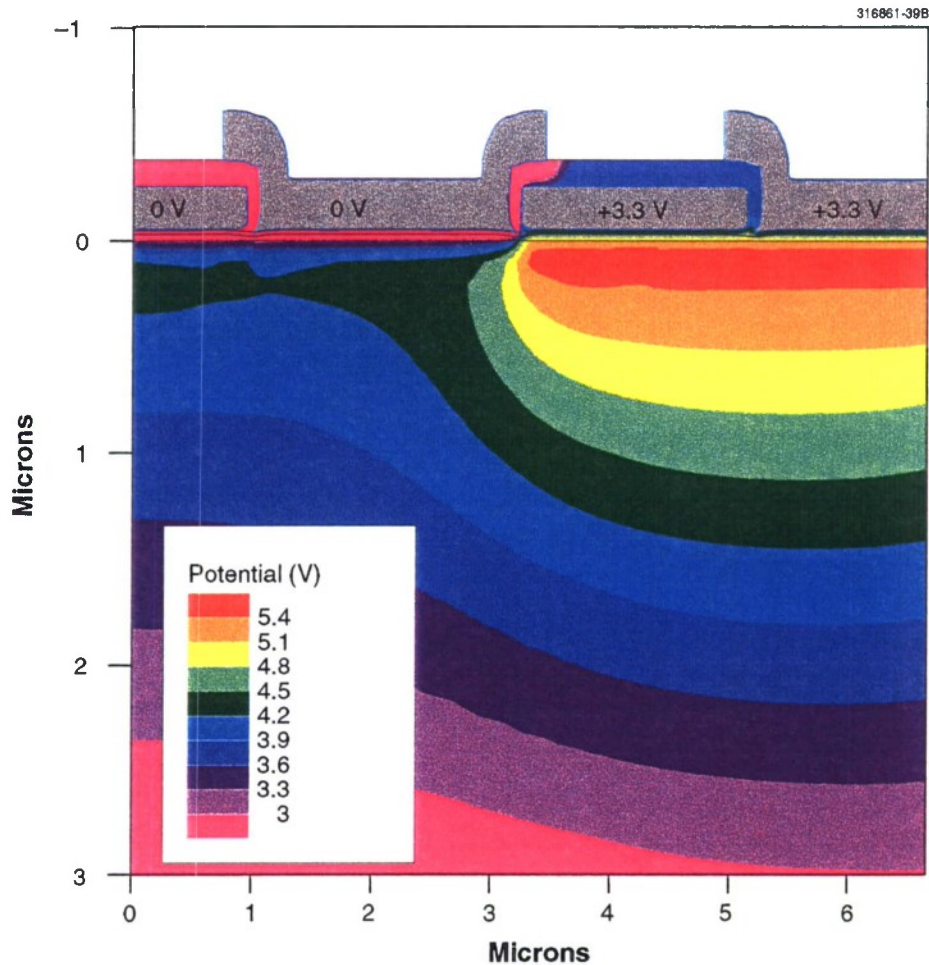
Figure 7-2. Simulated two-dimensional potential profiles for a +3.3-V four-phase CCD with arsenic buried-channel implant of 200-keV energy and 1.25×10^{12}-cm^{-2} dose.

gates with no potential "bumps" evident which would impede charge transfer. Figure 7-3 illustrates the simulated potential, dopant, and electron concentration profiles as a function of depth under a CCD gate. Again, simulations confirm that a potential barrier to the surface maintains buried-channel operation, and potential barriers exist between 3.3- and 0-V biased gates. The integrated simulated electron concentration profile predicts a 5.3×10^{11} cm^{-2} full well capacity.
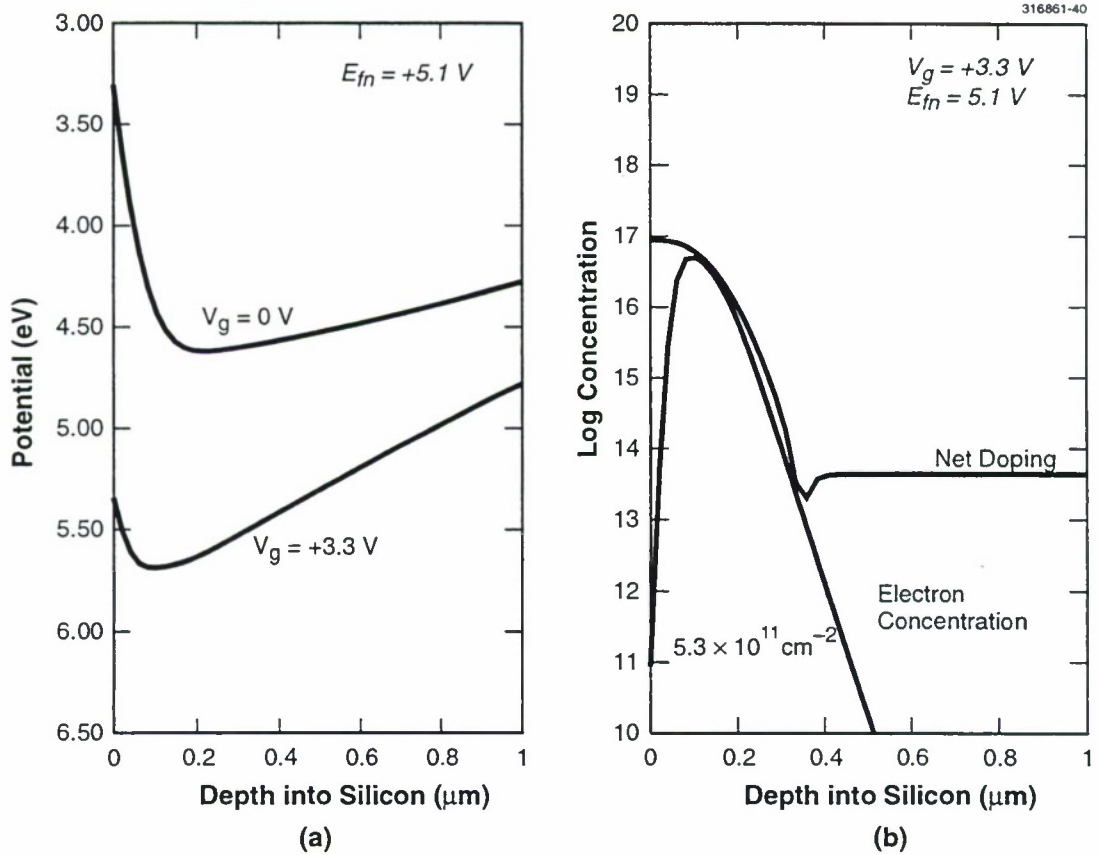
Figure 7-3. Simulated (a) potential and (b) doping and electron concentration profiles under high ($V_g = +3.3$ V) and low ($V_g = 0$ V) CCD gates for an arsenic buried-channel implant of 200-keV energy and 1.25×10^{12}-cm^{-2} dose.

The selection of substrate material was critical to maintain high CCD spectral response and charge-transfer efficiency (CTE) without degradation from the rapid thermal processing necessary for CMOS dopant profile control. To achieve high quantum efficiency, depletion layer width in the CCD must be comparable to maximum absorption depth of the targeted spectral range (uv to near infrared) to ensure efficient collection of photoexcited carriers. For a bias voltage of 3.3 V, a substrate resistivity of 100 Ω cm would give rise to high spectral response from ~0.4 to ~0.8 μm. A higher substrate resistivity would increase the CCD spectral range, as shown in Table 7-4. In order to ensure low dark current and high CTE of the CCD, low dislocation densities (<10/cm^2) and high crystalline quality of the Si substrate must be maintained throughout the entire fabrication process, including formation of the SOI layer. Thermally induced stress

TABLE 7-4
**Maximum Substrate N_B and Resistivity to Equate L_{abs} to Depletion Width
for a Particular λ at 3.3-V Bias, at a Temperature of 300 K**

Wavelength λ (μm)	Absorption Depth L_{abs} (μm)	Doping Density N_B (cm^{-3})	Resistivity (Ω cm)
0.90	22.9	1.0×10^{13}	1000
0.80	8.1	8.3×10^{13}	100
0.75	5.3	2.0×10^{14}	60
0.40	0.4	3.9×10^{16}	0.3

during SOI formation and circuit fabrication must be minimized so as not to cause slip or dislocation generation in the substrate. Rapid thermal processing required in the SOI CMOS process to minimize dopant diffusion was identified as a potential source of defect generation in the substrate material.

Preliminary studies of SOI substrates were performed on 100-mm-diam SOI from IBIS, SiBond, and SEH (Accuthin). The material was evaluated by removing the SOI and buried-oxide (BOX) layer, and then subjecting the SOI substrates to a Schimmel defect etch to decorate dislocations. As controls, bare prime Si wafers, as well as wafers that showed slip from prior thermal processing, were included. Wafers were evaluated using both optical microscope and scanning electron microscope inspection. Dislocation etch pits, about 3–4 μm in diameter, in the intentionally slipped control wafer were readily observed. In the SOI substrate materials, no etch pits were observed and an upper limit of dislocation density of 10/cm^2 was established. However, the defect decorative etch did reveal significant differences in the surface morphologies. The IBIS SOI substrate exhibited a rough surface (rms roughness of several hundred angstroms) believed to be related to Si precipitates that form in the BOX near the BOX-substrate interface. The SiBond substrate showed small circular etch pits within a few millimeters of the wafer edge but otherwise appeared smooth and featureless, and the SEH substrate revealed a hazy surface, believed to be the result of a pre-bonding surface treatment. In summary, in all of the 100-mm material, the dislocation density was acceptable, but the observed surface roughness posed potential problems for efficient charge transfer in CCDs.

A second round of material evaluation was performed on 150-mm-diam SOI material manufactured by IBIS, SOITEC, and SEH. Schimmel etch studies of the SOI substrates again indicated etch pit densities of all materials to be <10/cm^2. As before, the IBIS substrate surfaces were noticeably rough. The SEH

material showed a much smoother surface than the older 100-mm-diam SEH material, but was still noticeably rougher than a control, an etched prime Si wafer. By comparison, the SOITEC substrate surface was smooth and featureless, and comparable in quality to the control. Elemental contamination analysis of the substrate surfaces was performed using total x-ray fluorescence and secondary ion mass spectrometry. The only significant contaminant observed was B, to varying degrees in all the samples. Spreading resistance analysis, used to confirm this finding, showed in fact that surface layer buildup of boron was electrically active in the SOITEC and SEH material and not in the IBIS material, as shown in Figure 7-4. We concluded after discussions with SOI vendors that the boron was introduced into the SOI substrate by contamination from clean room high-efficiency particulate air (HEPA) filters containing borosilicate glass. SOITEC was confident that the unintentional surface boron doping could be eliminated simply by minimizing exposure of SOI wafers to HEPA-filtered air, by reducing elapsed time between process steps involved in manufacturing SOI material.

Additional rapid thermal processing testing was performed by subjecting samples to a 30-s, 950°C cycle necessary for dopant activation in the SOI CMOS process. The test wafers included a bare float-zone (FZ) Si wafer, and partially processed CCDs fabricated on both epi Si on Czochralski (CZ) and FZ substrates. The thermally cycled wafers, together with control CCD wafers not subjected to the rapid thermal
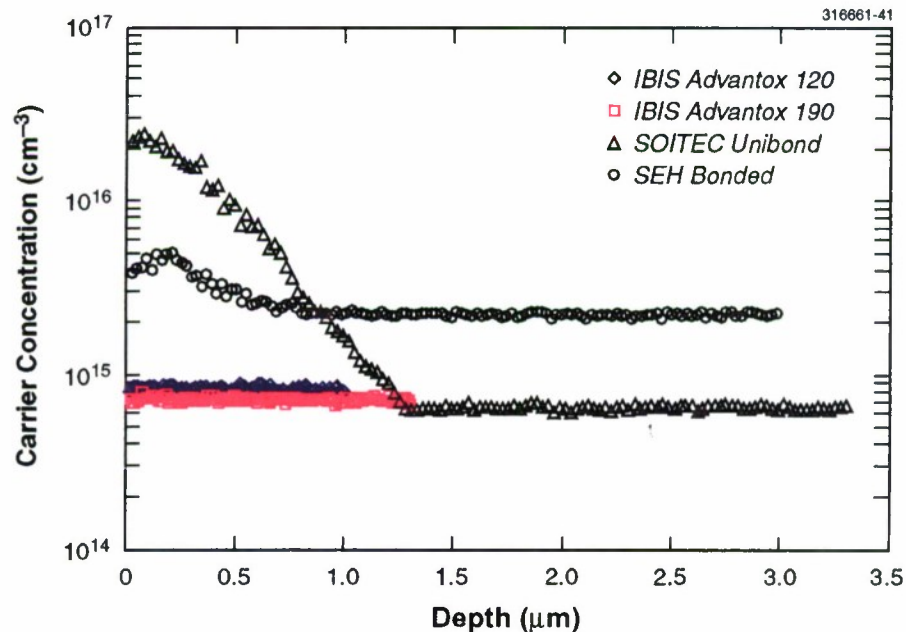

Figure 7-4. Carrier concentration vs depth for various silicon-on-insulator (SOI) substrates.

processing cycle, were stripped back to bare substrates, defect etched, and carefully inspected. In all cases, there was no evidence that rapid thermal processing gave rise to dislocation generation that would affect CCD performance. In the bare Si FZ substrate, special attention was focused near the wafer edge, where slip generation was the most likely to occur; and again, no dislocation etch pits were observed.

Based on the results of SOI substrate evaluation, we procured SOITEC Unibond SOI material on two different types of substrates, 200-Ω cm epi Si on CZ and 200-Ω cm FZ substrates. In comparison to the epi material the FZ substrate with higher resistivity offers a wider spectral range, but is more susceptible to thermal stress defect generation, which could adversely affect CCD performance. During manufacture of the SOI material, SOITEC took precautions to minimize boron contamination and utilized a low thermal stress procedure to process the wafers. Upon receipt of the material, spreading resistance profiles extending into the substrate from the BOX/substrate interface were measured, as shown in Figure 7-5, verifying that excess boron doping had indeed been eliminated.

The purpose of the first design iteration is to demonstrate feasibility of the integrated CCD/CMOS SOI technology. Figure 7-6 depicts the die layout for the first integrated CCD/CMOS SOI fabrication run. The design includes two CCD imagers with frame-transfer architecture, one with $(15 \ \mu m)^2$ pixels and the
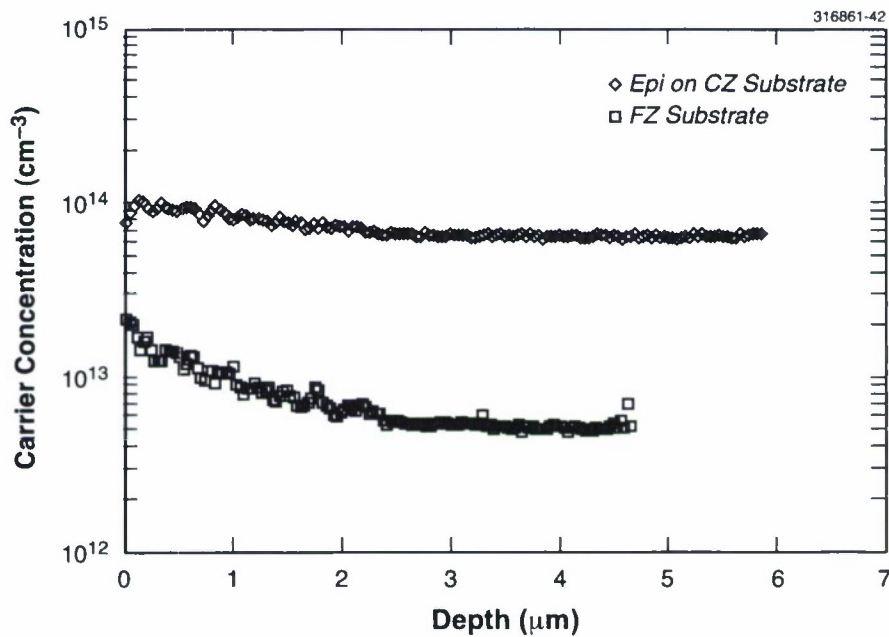

Figure 7-5. Carrier concentration vs depth for recently acquired SOITEC Unibond SOI.

316861-43
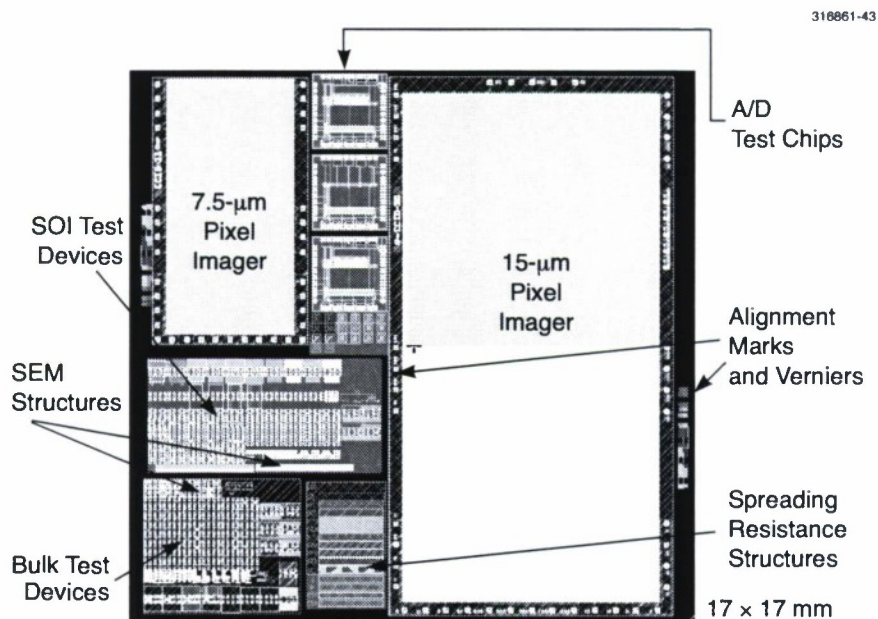
Figure 7-6. Die layout for first integrated CCD/CMOS process run. The reticle size is 17 × 17 mm.

other with $(7.5\,\mu m)^2$ pixels. In addition, the reticle includes representative analog-to-digital conversion test circuits as well as a full complement of bulk and SOI test structures for SPICE and process parameter extraction.

V. Suntharalingam   C. K. Chen
J. A. Burns   C. L. Keast
P. W. Wyatt

REFERENCES

1.   Solid State Research Report, Lincoln Laboratory, MIT, 1996:2, p. 35.

2.   Solid State Research Report, Lincoln Laboratory, MIT, 1997:3, p. 22.

3.   Solid State Research Report, Lincoln Laboratory, MIT, 1997:1, p. 45.

REPORT DOCUMENTATION PAGE

Public reporting burden for this collection of information is estimated to average 1 hour per response, including the time for reviewing instructions, searching existing data sources, gathering and maintaining the data needed, and completing and reviewing the collection of information. Send comments regarding this burden estimate or any other aspect of this collection of information, including suggestions for reducing this burden, to Washington Headquarters Services, Directorate for Information Operations and Reports, 1215 Jefferson Davis Highway, Suite 1204, Arlington, VA 22202-4302, and to the Office of Management and Budget, Paperwork Reduction Project (0704-0188), Washington, DC 20503.

1. AGENCY USE ONLY (Leave blank)	2. REPORT DATE 15 May 1998	3. REPORT TYPE AND DATES COVERED Quarterly Technical Report, 1 February–30 April 1998	
4. TITLE AND SUBTITLE Solid State Research			**5. FUNDING NUMBERS** C — F19628-95-C-0002 PR — 221
6. AUTHOR(S) David C. Shaver			
7. PERFORMING ORGANIZATION NAME(S) AND ADDRESS(ES) Lincoln Laboratory, MIT 244 Wood Street Lexington, MA 02420-9108			**8. PERFORMING ORGANIZATION REPORT NUMBER** 1998:2
9. SPONSORING/MONITORING AGENCY NAME(S) AND ADDRESS(ES) HQ Air Force Materiel Command AFMC/STSC Wright-Patterson AFB, OH 45433-5001			**10. SPONSORING/MONITORING AGENCY REPORT NUMBER** ESC-TR-97-136

11. SUPPLEMENTARY NOTES

None

12a. DISTRIBUTION/AVAILABILITY STATEMENT Approved for public release; distribution is unlimited.	12b. DISTRIBUTION CODE

13. ABSTRACT (Maximum 200 words)

This report covers in detail the research work of the Solid State Division at Lincoln Laboratory for the period 1 February–30 April 1998. The topics covered are Quantum Electronics, Electro-optical Materials and Devices, Submicrometer Technology, High Speed Electronics, Microelectronics, Analog Device Technology, and Advanced Silicon Technology. Funding is provided by several DoD organizations — including the Air Force, Army, BMDO, DARPA, Navy, NSA, and OSD — and also by the DOE, NASA, and NIST.

14. SUBJECT TERMS				15. NUMBER OF PAGES 78
quantum electronics electro-optical devices materials research submicrometer technology	high-speed electronics microelectronics analog device technology advanced silicon technology	bioaerosol sensor analog optical links tapered lasers excimer lasers	field-emitter arrays charge-coupled devices chirp filters	16. PRICE CODE

17. SECURITY CLASSIFICATION OF REPORT	18. SECURITY CLASSIFICATION OF THIS PAGE	19. SECURITY CLASSIFICATION OF ABSTRACT	20. LIMITATION OF ABSTRACT
Unclassified	Same as Report	Same as Report	Same as Report